NACA

RESEARCH MEMORANDUM

FORCE, MOMENT, AND PRESSURE-DISTRIBUTION CHARACTERISTICS

OF RECTANGULAR WINGS AT HIGH ANGLES OF ATTACK

AND SUPERSONIC SPEEDS

By William C. Pitts

Ames Aeronautical Laboratory
Moffett Field, Calif.

NATIONAL ADVISORY COMMITTEE
FOR AERONAUTICS

WASHINGTON

February 13, 1956
Declassified April 12, 1961

NATIONAL ADVISORY COMMITTEE FOR AERONAUTICS

RESEARCH MEMORANDUM

FORCE, MOMENT, AND PRESSURE-DISTRIBUTION CHARACTERISTICS

OF RECTANGULAR WINGS AT HIGH ANGLES OF ATTACK

AND SUPERSONIC SPEEDS

By William C. Pitts

SUMMARY

Experimental force and moment data are presented for rectangular wings of aspect ratios 1, 2, and 3. The angle-of-attack range is about $\pm 42^\circ$ and the Mach number range is 1.45 to 3.36. Experimental pressure-distribution data from NACA RM A54D19 and RM A54J12 are used to correlate the force data. It is found that shock-expansion theory adequately predicts the span load distribution in the two-dimensional flow region below the shock-detachment angle. In the absence of an adequate theory for the tip region, a semiempirical method is developed for estimating the span load distributions. With this method, the span load distribution and total normal force can be estimated up to the shock-detachment angle. Another procedure correlates the lift curves within ± 5 percent up to the maximum lift coefficient for aspect ratios greater than 1.

INTRODUCTION

The problems of the supersonic flight of airplanes and missiles at large angles of attack have recently received increased attention as a result of the high altitudes currently encountered by such aircraft as well as the higher altitudes contemplated in the future. For missiles, these problems are of increased importance because it is practical and desirable to utilize high normal accelerations for intercepting fast targets. Relatively little information is available for use in the design of bodies, wings, and complete configurations operating at large angles. For bodies, the work of Allen and Perkins, reference 1, permits estimation of the important over-all effects of angle of attack on lift and moment. For wings, not much information is available besides the work of Gallagher and Mueller, reference 2, and Mayer, reference 3, for estimating the aerodynamic characteristics near maximum lift at supersonic speeds. Some

data on the longitudinal aerodynamic characteristics of a complete missile
configuration at high angles of attack are available in reference 4.

   To fill this need for information on aerodynamic characteristics at
high angles of attack, a series of tests were preformed in the Ames 1-
by 3-foot supersonic wind tunnel. This program investigated the effects
of high angles of attack on wings, bodies, wing-body combinations, and
on the wake behind the wings. Data reports on the pressure distributions
on triangular and rectangular wings for several Mach numbers have been
published (refs. 5 and 6). Applications of the data of this investigation
have been made to the study of loads on wings and wing-body combinations
in reference 7 and to considerations of stability and control in refer-
ence 8. Another report of this series, reference 9, discusses some vortex
wake characteristics of an inclined body of revolution. The present
report presents an analysis of the rectangular-wing data of references 5
and 6 as well as of some unpublished force data obtained during the same
program. The data are compared with theory, gaps in the available theory
are pointed out and, where possible, methods are presented to fill them.

<div align="center">SYMBOLS</div>

A aspect ratio

A_r reduced aspect ratio, $\frac{2s}{\eta^*}$

c wing chord

C_b root-bending-moment coefficient, $\frac{M_b}{q_\infty Ss}$

C_D drag coefficient, $\frac{D}{q_\infty S}$

C_L lift coefficient, $\frac{L}{q_\infty S}$

$C_{L_{\alpha_0}}$ lift-curve slope at $\alpha = 0$

C_m pitching-moment coefficient, $\frac{M_m}{q_\infty Sc}$

c_{n_s} contribution to local normal-force coefficient of one surface of wing due to angle of attack, $\frac{1}{c}\int_0^c \left(P - P_{\alpha=0}\right)dx$

$\dfrac{c_{n_s}}{c_{n_s}*}$ ratio of local normal-force coefficient in tip region to that in two-dimensional region for one surface of wing

C_N normal-force coefficient, $\dfrac{N}{q_\infty S}$

d   shaft diameter

D   drag force on semispan wing

k_u, k_l empirical constants for upper and lower surfaces, respectively

L   lift force on semispan wing

M   local Mach number

M_b bending moment on semispan wing about wing root

M_m pitching moment on semispan wing about wing midchord

N   normal force on semispan wing

p   local static pressure

p_w reference static pressure

P   pressure coefficient, $\dfrac{p - p_\infty}{q_\infty}$

q   dynamic pressure

R   Reynolds number per in.

s   wing semispan

S   plan-form area of semispan wing

t   local thickness of wing

V   velocity

x   variable distance from wing leading edge

$\bar{x}$ distance from wing leading edge to center-of-pressure position

y   variable distance from wing root

$\bar{y}$ distance from wing root to center-of-pressure position

α wing angle of attack, deg

α_d angle of attack at shock detachment

β $\sqrt{M_\infty{}^2 - 1}$

η variable distance from wing tip, s - y

$\eta*$ distance from wing tip to point of intersection of tip Mach
          wave with wing trailing edge

Subscripts

B   values predicted by Busemann theory

l lower surface

max   maximum

min   minimum

u   upper surface

∞ free stream

Superscript

*   theoretical two-dimensional value

EXPERIMENTAL CONSIDERATIONS

Wind Tunnels

Both of the Ames 1- by 3-foot supersonic wind tunnels were used in
this investigation. The No. 1 tunnel is a single-return, continuous-
operation, variable-pressure wind tunnel that has a Mach number range
from 1.2 to 2.5. The No. 2 tunnel is an intermittent-operation,
nonreturn, variable-pressure wind tunnel that has a Mach number range
from 1.2 to 4.0. In both tunnels the Mach number is changed by varying
the contour of flexible plates which comprise the top and bottom walls
of the tunnels. The No. 1 tunnel was used to obtain the $M_\infty = 1.45$,
1.97, and 2.46 pressure-distribution data and the $M_\infty = 1.45$ force data.
The No. 2 tunnel was used to obtain the $M_\infty = 3.36$ pressure data and the

M_∞ = 1.96, 2.43, and 3.36 force data. Except for M_∞ = 3.36 which is
out of the range of the No. 1 tunnel, the choice of tunnels was made on
the basis of availability of the tunnels at the time the tests were
conducted.

Models and Supports

The pressure-distribution wings and their supports are described in
references 5 and 6. Sketches and dimensions of all wings tested are
shown in figure 1. The wing section is formed by a circular arc to the
midchord and a parabolic arc to the trailing edge. The trailing-edge
thickness is 50 percent of the maximum thickness. The semivertex angle
at the leading edge is 5.7°. Two 5-percent-thick, rectangular wings of
aspect ratio 2 were used for the pressure-distribution tests. The two
wings were identical except that the root of one of them was thickened.
The effect of thickening the wing root was investigated because such
thickening is generally required for supersonic, all-movable wings to
maintain structural integrity between the comparatively thin wing and a
large hinge shaft. The pressure-distribution data from the unthickened-
root wing are used in this report. The four rows of orifices shown in
figure 1 are all located on one surface at 2.5, 25.0, 56.3, and 87.5
percent of the semispan from the wing root.

The force measurements were made on a side-support balance which is
described in detail in reference 10. Force measurements were made on
three 4-percent-thick, all-movable, rectangular wings of aspect ratios
1, 2, and 3 with thickened roots. Force tests were made for a fourth
wing that was identical to the aspect-ratio-1 wing except that it had no
thickened root. The wing section for the force tests is formed by one
circular arc. The trailing-edge thickness is 50 percent of the maximum
thickness. The semivertex angle at the leading edge is 3.9°.

All wings were mounted on a boundary-layer plate that served both
as a flow reflection plane and as a means of placing the wings in a
region free of tunnel-wall boundary layer. The boundary-layer plate is
described in detail in reference 10. Except for the unthickened-root
pressure-distribution wing, a 0.005- to 0.009-inch clearance gap was
allowed between the models and the boundary-layer plate to permit free
rotation. The unthickened-root pressure-distribution wing was mounted
rigidly on a turntable that was inset in the boundary-layer plate.

Range of Test Variables

The force measurements were made at Mach numbers of 1.45, 1.96,
2.43, and 3.36. The pressure-distribution models were tested at Mach

numbers of 1.45, 1.97, 2.46, and 3.36. The differences in Mach number
for the two types of tests are due to slight differences between the two
wind tunnels used. The force measurements were made for angles of attack
up to the maximum deflection of the balance, 42°, except for a few cases
in which the model support fouled 2° or 3° below this angle. For the
larger wings at the lower Mach numbers, the wind tunnel choked at angles
of attack considerably below 42°. For this reason the A = 1 wing was
scaled down to a span of 1.5 inches for tests at $M_\infty = 1.45$. The angle-
of-attack ranges for the pressure-distribution tests were about the same
as for the force measurements. The Reynolds number was varied but no
significant effects were observed. The Reynolds number for the data
presented ranged from 0.44×10^6 per inch to 0.86×10^6 per inch.

Reduction of Data

The pressure-distribution data were reduced to the coefficient form

$$P = \frac{p - p_\infty}{q_\infty} = \frac{p - p_W}{q_\infty} - \frac{p_\infty - p_W}{q_\infty}$$

where $(p - p_W)/q_\infty$ was the measured quantity and $(p_\infty - p_W)/q_\infty$ was the
correction obtained from surveys of the wind-tunnel air stream. This
correction was essentially zero for $M_\infty = 1.45$ and 2.46, but for
$M_\infty = 1.97$ it was approximately 0.02 and for $M_\infty = 3.36$ it was approxi-
mately 0.01. Span loading and total forces on the wing were obtained
from the pressure coefficients by numerical integration. Since the
pressure orifices were all on one surface of the wing, it was necessary
to add the pressures for the wing at corresponding positive and negative
angles of attack to obtain the total forces. Further details of the
numerical integration procedure are given in references 5 and 6.

All force and moment data measured on the balance were reduced to
the usual coefficient form. The plan-form area of the semispan wing
was used as the reference area. The plots of C_N and C_L against α
were corrected for small errors in α (of the order of ±0.1°) by
shifting the curves along the α axis until they passed through the
origin.

Accuracy of Data

From an examination of the inaccuracy in setting the model angle of
attack, the variations from constant test conditions, and the ability to
repeat the pressure data in reruns at $R = 0.44 \times 10^6$ per inch, it was
concluded that the errors in measuring the pressure coefficients were
about ±0.005 for all Mach numbers. The errors in the integrated forces

should be less than this because of the random nature of the errors in the pressure coefficients. A similar analysis of the balance force data showed an uncertainty in C_L of ±0.005, in C_D of ±0.002, in C_m of ±0.002, and in C_b of ±0.01. To compare force and pressure-distribution measurements, force measurements were made on the pressure-distribution wing for $M_\infty = 1.97$. It was found that the two methods of measurement agreed within the above accuracy.

Besides the question of the accuracy of the measurements, two other questions arise regarding the validity of the data: First, how well does the semispan-model data represent the data for a full-span model, and second, what is the effect of the thickened root on the force test wings? Three factors indicate that the boundary-layer plate does not interfere seriously with the pressure distribution and therefore gives valid full-span data: First, the pressure-distribution measurements in the wing-plate juncture check with shock-expansion theory within its range of applicability. Second, comparison of the pressures for the $y/s = 0.025$ and 0.250 stations shows that the boundary-layer plate does not alter the flow in the two-dimensional region. Third, below the shock-detachment angle there is no significant Reynolds number effect on the pressure distribution in the wing-plate juncture. Above the shock-detachment angle the Reynolds number effect is small and limited to the wing-plate juncture. (For further details, see refs. 5 and 6.) The second question was answered by comparing the results for corresponding wings with and without thickened roots. It was found that thickening the root causes some loss of lift in the root, but the pressures outboard of the root were only slightly affected. In general, this loss of lift due to the thickened root caused less than a 3-percent loss in the total lift for the aspect-ratio-1 wings. An even smaller loss would be expected for the higher aspect-ratio wings.

EXPERIMENTAL RESULTS

The pressure-distribution data for the entire range of variables tested are tabulated in references 5 and 6 in the form of pressure coefficients, integrated forces, and center-of-pressure positions. Only the pressure-distribution data that are necessary for the correlation method to be discussed are presented here. Since the force data have not previously been published, the lift curves, drag polars, pitching-moment curves, and root-bending-moment curves are presented in figures 2, 3, 4, and 5 for all Mach numbers and aspect ratios tested.

Figures 2, 3, and 4 show that there can be large effects of aspect ratio on C_L, C_D, and C_m. The effect of aspect ratio diminishes as the Mach number is increased, that is, as the effect of the wing tips relative to the entire wing diminishes. More will be said of the wing tips in the subsequent discussion.

Figures 2 through 5 show little effect of the thickened root section up to the shock-detachment angle. Above this angle, some effect is observed. Comparison of the pressure distributions in references 5 and 6 for several Reynolds numbers shows that this is due to a small viscous effect near the wing root.

Although $C_{L_{max}}$ is not reached in all cases, figure 2 appears to be consistent with the result of reference 2 that $C_{L_{max}}$ for rectangular wings is about 1.05. The two exceptions (for the aspect-ratio-1 wing at $M_{\infty} = 2.43$ and 3.36) are due to the effect of the thickened root section. This is shown most clearly by the $M_{\infty} = 3.36$ curve and to a lesser extent by the $M_{\infty} = 2.43$ curve. The effect of the thickened root should be smaller for the wings of aspect ratios 2 and 3 than for the aspect-ratio-1 wing.

The effects of Mach number and aspect ratio on some important aerodynamic parameters near $\alpha = 0$ are shown in the following tabulation:

$C_{L_{\alpha_0}}$			
M_{∞} \ A	1	2	3
1.45	2.03 (2.00)	3.00 (2.90)	3.28 (3.20)
1.96	1.73 (1.67)	2.04 (2.02)	2.12 (2.14)
2.43	1.55 (1.40)	1.73 (1.60)	1.75 (1.67)
3.36	1.17 (1.05)	1.24 (1.15)	1.23 (1.18)

$(\bar{x}/c)_{\alpha=0}$			
M_{∞} \ A	1	2	3
1.45	0.33 (.35)	0.40 (.45)	0.44 (.47)
1.96	.41 (.43)	.45 (.47)	.45 (.48)
2.43	.42 (.45)	.45 (.48)	.45 (.49)
3.36	.45 (.47)	.45 (.49)	--- (.49)

$(C_D)_{min}$			
M_{∞} \ A	1	2	3
1.45	0.016	0.018	0.020
1.96	.012	.014	.015
2.43	.010	.011	.012
3.36	.007	.007	.008

$(L/D)_{max}$			
M_{∞} \ A	1	2	3
1.45	4.9	6.2	6.1
1.96	5.7	5.7	5.8
2.43	5.8	5.8	5.8
3.36	6.4	6.7	5.7

The numbers in the parenthesis are linear-theory values. The trends in $C_{L_{\alpha_0}}$ with M_{∞} and A are well predicted by linear theory, but the

predicted magnitudes of the lift-curve slope are somewhat low. The center-of-pressure position predicted by linear theory is about 3 percent of the wing chord too far aft for all Mach numbers and aspect ratios. This is primarily due to second-order effects of thickness. The center-of-pressure travel with Mach number is primarily due to the wing-tip effect rather than section effects. This is apparent from the fact that the center-of-pressure position for the aspect-ratio-3 wing, which approaches a two-dimensional airfoil, is nearly constant. Regarding $(L/D)_{max}$, it is not surprising that no general trends occur since the drag due to the lift and $C_{D_{min}}$ have opposite effects upon $(L/D)_{max}$ as Mach number and aspect ratio vary.

CORRELATION AND DISCUSSION

Basic Physical Phenomena

Before discussing the method used to correlate the rectangular-wing data, it is well to describe first some of the basic physical phenomena of the flow over a three-dimensional, rectangular wing. A sketch of an aspect-ratio-2 semispan wing is shown in figure 6. The estimated Mach waves from the wing tip for $M_{\infty} = 1.97$ are shown for several angles of attack. The curvature of the Mach waves is due to the curvature of the wing surface and is obtained by computing the local Mach angle by shock-expansion theory. For $\alpha = 0^{\circ}$ the Mach waves are identical on the upper and lower surfaces, due to the symmetry of the wing. However, as the angle of attack changes the Mach waves move across the wing surface. On the upper surface the local Mach number increases with angle of attack so that the Mach wave moves toward the tip. On the lower surface the local Mach number decreases and the Mach wave fans out so that the tip influences more of the wing as the angle of attack increases. Since this movement of the tip Mach wave causes the aspect ratio of the wing effectively to vary with angle of attack, a quantity corresponding to the conventional effective aspect ratio, βA, is defined:

$$A_r \equiv \frac{2s}{\eta^*}$$

where A_r will be called the reduced aspect ratio[1] and η^* is the distance from the wing tip to the point of intersection of the tip Mach wave with the wing trailing edge. From the previous discussion it is apparent that A_r is a function of α and that it is larger on the upper surface than on the lower surface. These points are important to the subsequent discussion.

---

[1]For a flat plate at zero angle of attack, A_r is equal to the conventional effective aspect ratio, βA.

When the angle of attack increases beyond the point at which the tip Mach wave is coincident with the wing leading edge ($\alpha_d = 17^o$ in fig. 6) the shock wave becomes detached. The shock-wave-attached and the shock-wave-detached regimes will be discussed separately. For the attached regime the flow can be further subdivided into two regions on the wing surface. The region inboard of the point of intersection of the tip Mach wave with the wing trailing edge will be designated the two-dimensional region, and the region outboard of this point will be designated the tip region. (The extent of these regions will of course vary with angle of attack and it will be different on the upper and lower surfaces.) The span load distributions for these two regions will be treated independently. The span load distribution for the entire wing will then be the load distributions of these two regions joined at their common boundary.

Attached Regime

Load distribution in two-dimensional region.- Two-dimensional, shock-expansion theory is compared with experimental pressure distribution data in figure 7. The agreement, which is typical for all Mach numbers of this test, shows that the existing shock-expansion theory adequately predicts the pressures and hence the loads in the two-dimensional region. The discrepancy near the leading edge of the root in figure 7(b) is due to a small, localized effect of the boundary-layer plate.

Load distribution in tip region.- There is no theory available that adequately predicts the load in the tip region for angles of attack up to the shock-detachment angle. Busemann's linearized, conical-flow, tip theory (ref. 11) is compared with an experimental spanwise pressure distribution in figure 8. It is apparent that the linear theory has two shortcomings: One, the predicted magnitude of the pressure in the two-dimensional region is low, as might be expected; and, two, the position of the Mach wave is predicted incorrectly, as shown by the insert. An obvious modification is to stretch the Busemann theory as shown by the dashed curve so that it agrees with two-dimensional, shock-expansion theory at the correct Mach wave position. (This is essentially the method used in ref. 12.) However, the experimental data are still not well predicted. A linearized, conical-flow theory that considers the effect of the wing vortices is presented in reference 13. However, this theory is not in good agreement with the experimental results of this investigation as shown by figure 9. In this figure the theoretical and experimental values of the local loading (both surfaces) are normalized by the two-dimensional section loading and plotted against the usual conical parameter $\beta\eta/x$. For $\beta\alpha = 0$ there are no vortices present and the theory reduces to that of Busemann. It is apparent that the flow in the tip region is not conical from the fact that when plotted against the

conical parameter, $\beta\eta/x$, the experimental loading pressures taken along the $\eta/s = 0.125$ station differ from those taken along the $\eta/s = 0.437$ station. Thus the poor agreement with the conical-flow theories of references 11 and 13 is not surprising and a nonconical theory is needed. The nonconical nature of the flow is probably due primarily to the fact that the surface of the wing is not conical at the tip. Better agreement with these theories should be obtained for surfaces that are conical from the leading edge of the wing tip.

In the absence of an adequate theory, a semiempirical method was formulated for predicting the span loading in the tip region. Figure 10 shows the basis of this method. The experimental section load distribution in the tip region is presented in normalized form for both the upper and lower surfaces of the wing. The abscissa, $\eta/\eta*$, is the fraction of the distance from the wing tip, $\eta/\eta* = 0$, to the total width of the tip region. The dashed curves are approximate fairings of the experimental data for the lower surface of the wing. The shape of this family of curves was based on data at all test Mach numbers and angles of attack below shock detachment. It is apparent that the loading increases more rapidly with α in the tip region than in the two-dimensional region, and that it approaches rectangular loading as pointed out in references 5 and 6. The solid curves show the variation due to angle of attack of $c_{n_s}/c_{n_s}*$ at a fixed geometric position on the wing, $y/s = 0.875$. The upper and lower surface curves cross near the Busemann theory curve. This is to be expected since, by symmetry, the two experimental curves must cross at $\alpha = 0°$, and Busemann's theory becomes exact as α approaches zero. The similarity of the span loading curves in the tip region suggests the following semiempirical method: (1) Use Busemann's theory to give the basic shape of the loading for $\alpha = 0°$. (2) Use shock-expansion theory to give the absolute magnitudes at point (1,1) in figure 10. (3) Use an empirical correction to account for the effect of α. This empirical correction will in general be a small percentage of the loading, so that great accuracy in the correction is not necessary.

The form of this empirical correction can be seen from figure 11 where $c_{n_s}/c_{n_s}*$ is plotted against α for several values of $\eta/\eta*$ and for several Mach Numbers. The value of $c_{n_s}/c_{n_s}*$ at $\alpha = 0$ is the Busemann theory value and the other points are obtained from faired curves of the type shown in figure 10. Figure 11 shows that $c_{n_s}/c_{n_s}*$ varies nearly linearly with α on the upper surface. Examination of these data for fixed values of α shows that $c_{n_s}/c_{n_s}*$ varies with Mach number approximately as $\beta^{-1/3}$. Thus $c_{n_s}/c_{n_s}*$ can be expressed as

$$\left(\frac{c_{n_s}}{c_{n_s}*}\right)_u = \left(\frac{c_{n_s}}{c_{n_s}*}\right)_B + k_u \beta^{-1/3}\alpha \qquad (1)$$

for the upper surface. This method of analysis of the data for the
lower surface shows that

$$\left(\frac{c_{n_s}}{c_{n_s}*}\right)_l = \left(\frac{c_{n_s}}{c_{n_s}*}\right)_B + k_l \beta^{3/2} \alpha^{1/\beta} \tag{2}$$

for the lower surface. The empirical constants k_u and k_l depend upon
$\eta/\eta*$ (fig. 12).[2] The value of $dc_{n_s}/d\alpha$ at $\alpha = 0^\circ$ given by equations (1)
and (2) is identical to that given by Busemann's linear theory. The
primary effects of thickness and section are accounted for in equa-
tions (1) and (2) by shock-expansion theory, both as to the magnitude
of the two-dimensional loading and as to the extent of the tip region.
Thickness will have some effect on the constants k_u and k_l but the
effect on the loading will be small for the thin wings considered. This
is particularly true for moderate and large angles of attack for which
the thickness effect is relatively small compared to the angle-of-attack
effect.

There remains the problem of combining the effects of two tip
regions when the influences of opposite wing tips overlap. Busemann's
method of adding decrements can be
used for reduced aspect ratios
greater than 1. However, this
method gives values that are too
low for reduced aspect ratios less
than 1. Thus, another method for
combining the wing tips must be
devised. Two conditions that are
required of this method are that
it agree with Busemann's theory
in its range of applicability and
that it always give zero loading
at the wing tips. These condi-
tions can be fulfilled by super-
imposing the span loadings of
each tip and taking the product
of the two loadings as the total
loading. This is clarified by
sketch (a). The upper part of
this sketch shows the Mach wave
pattern for a flat-surface wing
with a reduced aspect ratio less
than 1. The solid curves in the
lower part of the sketch show the

Sketch a
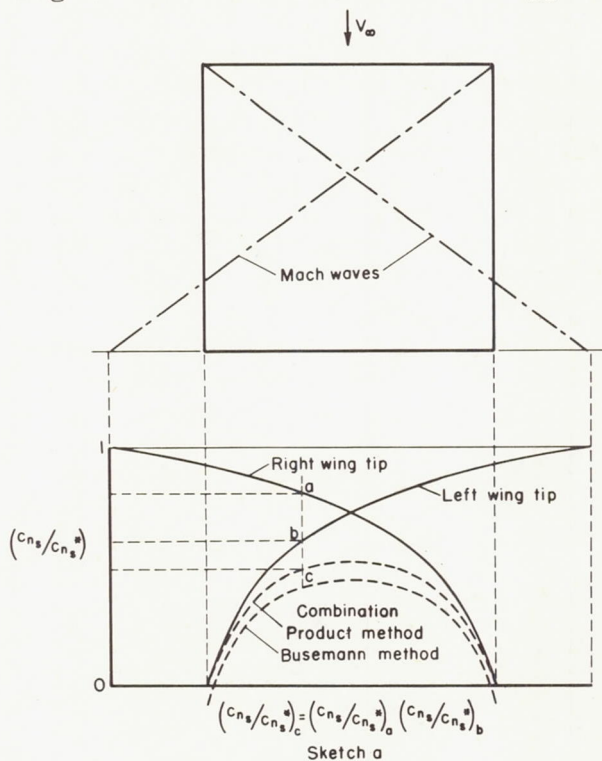
[2]No data were obtained for $0 \leq \eta/\eta* \leq 0.1$ so that no empirical
values for $k_{u,l}$ were obtained for this range. However, the loading
is zero at the wing tip so that the span loading can be faired through
this range as in figure 10.

reduced span loading that would exist on the two wing tips if there were no mutual interaction. The dashed curve labeled "product method" is the combined span loading. Any point, c, on this curve is obtained as the product of $c_{n_S}/c_{n_S}*$ at points a and b of the solid curves. The "Busemann Method" curve is low, because the reduced aspect ratio is less than 1. If the reduced aspect ratio curve were 1 or greater, the two combination curves would coincide at the wing tips and differ by, at most, 4 percent at the center section of the wing.

The degree of correlation is shown in figure 13 where correlation curves compare the predicted and experimental values of $c_{n_S}/c_{n_S}*$ for all Mach numbers tested. The figure shows that the empirical method correlates the span loading data for all Mach numbers within ±5 percent. The number of spanwise orifice stations on the rectangular pressure distribution wing that lie within the tip region depends upon the Mach number and angle of attack, but, in general, the stations at $y/s = 0.563$ and 0.875 are represented in figure 13. Thus, with the foregoing methods, the span load distribution in the tip region can be estimated within ±5 percent for thin rectangular wings at any angle of attack below the shock-detachment angle for the ranges of Mach numbers and aspect ratios of this investigation.

Total normal force.- The total normal-force coefficients were computed for the force test wings of this investigation by the semiempirical method of this report. In figure 14 the results are compared with the experimental force data which, as has been pointed out, are completely independent of the pressure-distribution data that were used to obtain the semiempirical method of correlation. In general, the agreement is good, both as to magnitude and as to the trends with Mach number, aspect ratio, and angle of attack.

In figure 14(a), the curvature of the predicted A = 1 curve near the shock-detachment angle is due to the limitations of the product method of combining wing tips at extremely low reduced aspect ratios. For all other calculations for figure 14 the reduced aspect ratio was large enough, up to within 1° or 2° of the shock-detachment angle,[3] that this difficulty was not encountered. The low experimental point in figure 14(d) for the aspect-ratio-1 wing at $\alpha = 30^\circ$ is due to the thickened root of the wing (see fig. 2).

In figure 15 a typical comparison is made between the semiempirical method and other methods of estimating the C_N vs. α curve. Except for very low angles of attack the three-dimensional, linear-theory curve is considerably low. At $\alpha = 0$ the slopes of the semiempirical curve and the linear-theory curve are essentially the same. Naturally, the two-dimensional, shock-expansion-theory curve is too high since tip effects are neglected. As the aspect ratio and/or the Mach number increase, the

---

[3]As the shock-detachment angle is approached, $A_r \longrightarrow 0$.

semiempirical curve and the stretched Busemann theory curve will approach
the two-dimensional curve.

Center-of-pressure position.- A qualitative story of the variation
of the center-of-pressure position with α can be formulated that is
consistent with the findings of the preceding sections. From figure 10
it is apparent that the span loading on both the upper and lower sur-
faces becomes more rectangular as the angle of attack increases. Hence
the center of pressure moves outboard with angle of attack, as shown in
figure 16. The exception at $\alpha = 30^{\circ}$ and 35° for $M_{\infty} = 3.36$ is due to
an unexplained reversal of the trend toward uniform loading near the
shock-detachment angle for this Mach number. The variation of the
chordwise center-of-pressure position cannot be explained quite so
simply because two effects oppose each other on the lower surface, which
contributes most of the lift at high angles of attack: (1) According to
shock-expansion theory the center of pressure moves rearward as α
increases for the airfoil section used in this investigation.[4] (2) The
effect of the tip Mach wave moving inboard with increasing α on the
lower surface is to cause the center-of-pressure position to move for-
ward. The net result of these two phenomena depends upon whether the
tip region or the two-dimensional region dominates the wing surface
area. Call the angle-of-attack range in which the two-dimensional
region dominates, Regime I, and the angle-of-attack range (for $\alpha < \alpha_d$)
in which the tip region dominates, Regime II. Regime III includes the
angles of attack above the shock-detachment angle. These regimes are
indicated in figure 16. In figure 16(c), for example, the center-of-
pressure position is in Regime I for $\alpha = 3^{\circ}$. Section effects cause
the center of pressure to move rearward until Regime II is entered at
about 13°. Then the tip effect predominates and the center-of-pressure
position moves forward. At the shock-detachment angle, $\alpha_d = 24^{\circ}$,
Regime III is entered and the center-of-pressure position again moves
rearward toward the wing midchord. In figure 16(a) the center-of-pressure
position skips Regime I and starts in Regime II because for this low
Mach number the tip region dominates even at small angles of attack. In
figure 16(d) the angle-of-attack range is barely large enough for the
shock wave to detach and Regime III is not apparent.

Detached Regime

Since there is no theory available for flow over wings at angles
of attack above the shock-detachment angle, the discussion of the
detached regime will be limited to pointing out interesting observations.

Details of flow.- A sketch of the flow over a wing with a detached
shock wave is shown in figure 17. The salient features of this sketch
are in accord with figure 18 which shows the Mach number variation over
[4]This is not true for all airfoil sections.

the wing surface for several free-stream Mach numbers and angles of
attack. These Mach number contours were obtained by assuming that the
stagnation streamline crossed the bow shock wave normally. Figure 18
shows that the stagnation point, M = 0, lies within 0.05c of the leading
edge. It also shows that there are two M = 1 lines as shown in figure
17. The foremost M = 1 line intersects the wing surface somewhere
between 0.05c on the lower surface where the flow is subsonic and 0.05c
on the upper surface where the flow is supersonic. It probably inter-
sects at the wing leading edge where a large expansion occurs. The
other M = 1 line intersects somewhere along the lower surface or in the
wake, depending upon the free-stream Mach number and angle of attack.
Between these M = 1 lines there is a region on the surface over which
the flow is subsonic. Another interesting feature of the flow shown by
figure 18 is that the local Mach number, and hence, the pressure on the
upper surface of the wing, is nearly constant. This is consistent with
the findings of Mayer, reference 3, that the pressure approaches a
uniform limiting value on the upper surface of wings at high angles of
attack. This limiting pressure coefficient was estimated to be 70 per-
cent of vacuum $(P = - 1/M_\infty^2)$.

Pressure distributions.- The chordwise distribution of the pressure
coefficient is plotted in figure 19 to show the effect of angle of
attack, spanwise location, and Mach number. The figure shows that above
the shock-detachment angle the pressure coefficient rises rapidly near
the leading edge of the lower surface. This feature, characteristic of
subsonic flow, is to be expected because of the subsonic region on the
lower surface of the wing shown in figure 17. On the upper surface of
the wing Mayer's limiting value, the dashed lines in the figure, gives
a fair estimate of the limiting pressure coefficient. However, there
is in general a considerable range of angles of attack between the
shock-detachment angle and the angles at which the limiting value is
approached.

Lift coefficient.- In figure 20 the lift curves are correlated
within ±5 percent of an average curve up to the maximum value of the
lift coefficient for all of the aspect ratios and Mach numbers tested
in this investigation. Some data from reference 2 are also included.
In this correlation it is assumed that the maximum value of the lift
coefficient is approximately the same for all Mach numbers and aspect
ratios, as is suggested by figure 2. The correlating parameter, $\alpha C_{L_{\alpha_0}}$
merely adjusts all lift curves so that they have the same slope at
$\alpha = 0$. Since the curves are forced to coincide at $\alpha = 0$, no data are
shown in the figure for the small angles. Thus, within the Mach number
and aspect-ratio range of this investigation, the lift curves of rectan-
gular wings can be predicted up to the maximum value of the lift coeffi-
cient if the lift curve slope at $\alpha = 0$ is known. It is quite possible
that this Mach number and aspect-ratio range can be extended. However,
it should be pointed out that a small decrease in $C_{L_{max}}$ was observed

as the aspect ratio decreased so that this correlation method is not dependable for A < 1.

CONCLUSIONS

Analysis of the force and pressure-distribution data from this investigation showed that for the Mach number range of 1.45 to 3.36 and the aspect ratio range of 1 to 3 the following conclusions can be drawn for rectangular wings:

1. Shock-expansion theory gives an adequate prediction of the pressure distribution and section loading in the two-dimensional region up to the shock-detachment angle.

2. The flow in the tip region is not conical. In the absence of a theory, a semiempirical method was developed that predicts the span load distribution near the wing tips and the total normal-force coefficient with engineering accuracy up to the shock-detachment angle.

3. The lift curves can be correlated within ±5 percent up to the maximum value of the lift coefficient for variations of Mach number between 1.45 and 3.36 and for aspect ratios greater than 1.

Ames Aeronautical Laboratory
        National Advisory Committee for Aeronautics
            Moffett Field, Calif., Nov. 9, 1955

REFERENCES

1. Allen, H. Julian, and Perkins, Edward W.: Characteristics of Flow
        Over Inclined Bodies of Revolution. NACA RM A50L07, 1951.

2. Gallagher, James J., and Mueller, James N.: Preliminary Tests to
        Determine the Maximum Lift of Wings at Supersonic Speeds.
        NACA RM L7J10, 1947.

3. Mayer, John P.: A Limit Pressure Coefficient and an Estimation of
        Limit Forces on Airfoils at Supersonic Speeds.
        NACA RM L8F23, 1948.

4. Spahr, J. Richard: Longitudinal Aerodynamic Characteristics to
        Large Angles of Attack of a Cruciform Missile Configuration at a
        Mach Number of 2. NACA RM A54H27, 1954.

5. Kaattari, George E.: Pressure Distributions on Triangular and
     Rectangular Wings to High Angles of Attack - Mach Numbers 1.45 and
     1.97. NACA RM A54D19, 1954.

6. Kaattari, George E.: Pressure Distributions on Triangular and
     Rectangular Wings to High Angles of Attack - Mach Numbers 2.46 and
     3.36. NACA RM A54J12, 1955.

7. Katzen, Elliott D., and Pitts, William C.: Load Distribution on
     Wings and Wing-Body Combinations at High Angles of Attack and
     Supersonic Speeds. NACA RM A55E17, 1955.

8. Kaattari, George E., Hill, William A., Jr., and Nielsen, Jack N.:
     Controls for Supersonic Missiles. NACA RM A55D12, 1955.

9. Jorgensen, Leland H., and Perkins, Edward W.: Investigation of Some
     Wake Vortex Characteristics of an Inclined Ogive-Cylinder Body at
     Mach Number 1.98. NACA RM A55E31, 1955.

10. Katzen, Elliott D., Kuehn, Donald M., and Hill, William A., Jr.:
     Investigation of the Effects of Profile Shape on the Aerodynamic
     and Structural Characteristics of Thin, Two-Dimensional Airfoils
     at Supersonic Speeds. NACA RM A54B08a, 1954.

11. Busemann, Adolf: Infinitesimal Conical Supersonic Flow.
     NACA TM 1100, 1947.

12. Czarnecki, K. R., and Mueller, James N.: An Approximate Method of
     Calculating Pressures in the Tip Region of a Rectangular Wing of
     Circular-Arc Section at Supersonic Speeds. NACA TN 2211, 1950.

13. Cheng, H. K.: Aerodynamics of a Rectangular Plate With Vortex
     Separation in Supersonic Flow. Jour. Aero. Sci., vol. 22, no. 4,
     Apr. 1955, pp. 217-226.
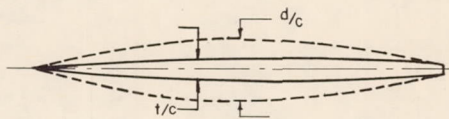
A	2
d/c	.156

A	1	2	3
d/c	.109	.156	.187

(d/c)   .400"
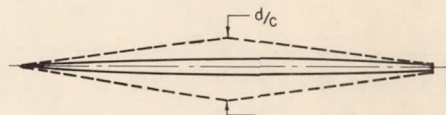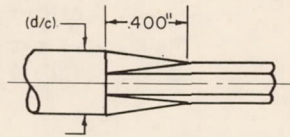
Rear view of
Thickened root wing

c=4.00"

.400"

s=4.00"

Thickened roots

.400"

c=2.67"
c=8.00"

s=4.00"
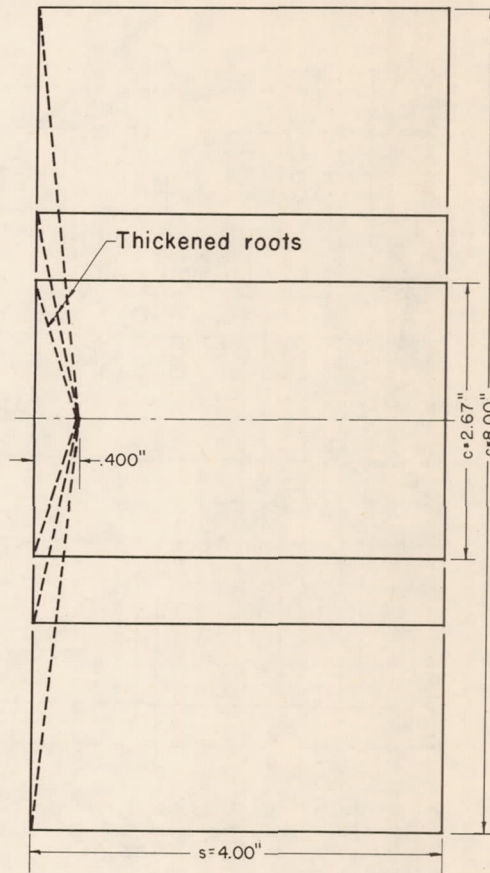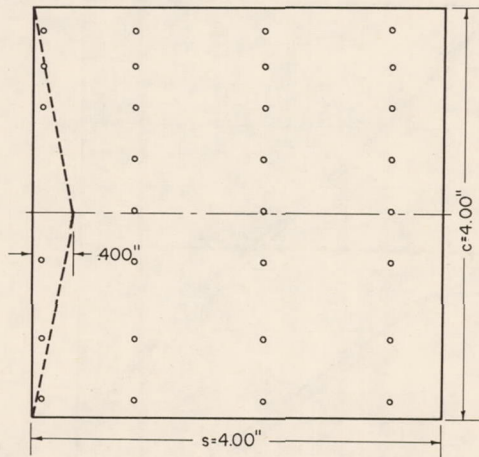
Note: s=1.5" for A=1 force test wing
for M=1.45

$$t/c = 2\left[\sqrt{(5.013)^2 - (x/c - .5)^2} - (4.988)\right]; 0 \leq x/c \leq 1/2$$

$$t/c = 2\left[.025 - .05(x/c - .5)^2\right]; 1/2 \leq x/c \leq 1$$

$$t/c = 2\left[\sqrt{(8.580)^2 - (x/c - .586)^2} - (8.560)\right]; 0 \leq x/c \leq 1$$

Pressure distribution wings

Force test wings

Figure 1.- Wing dimensions.
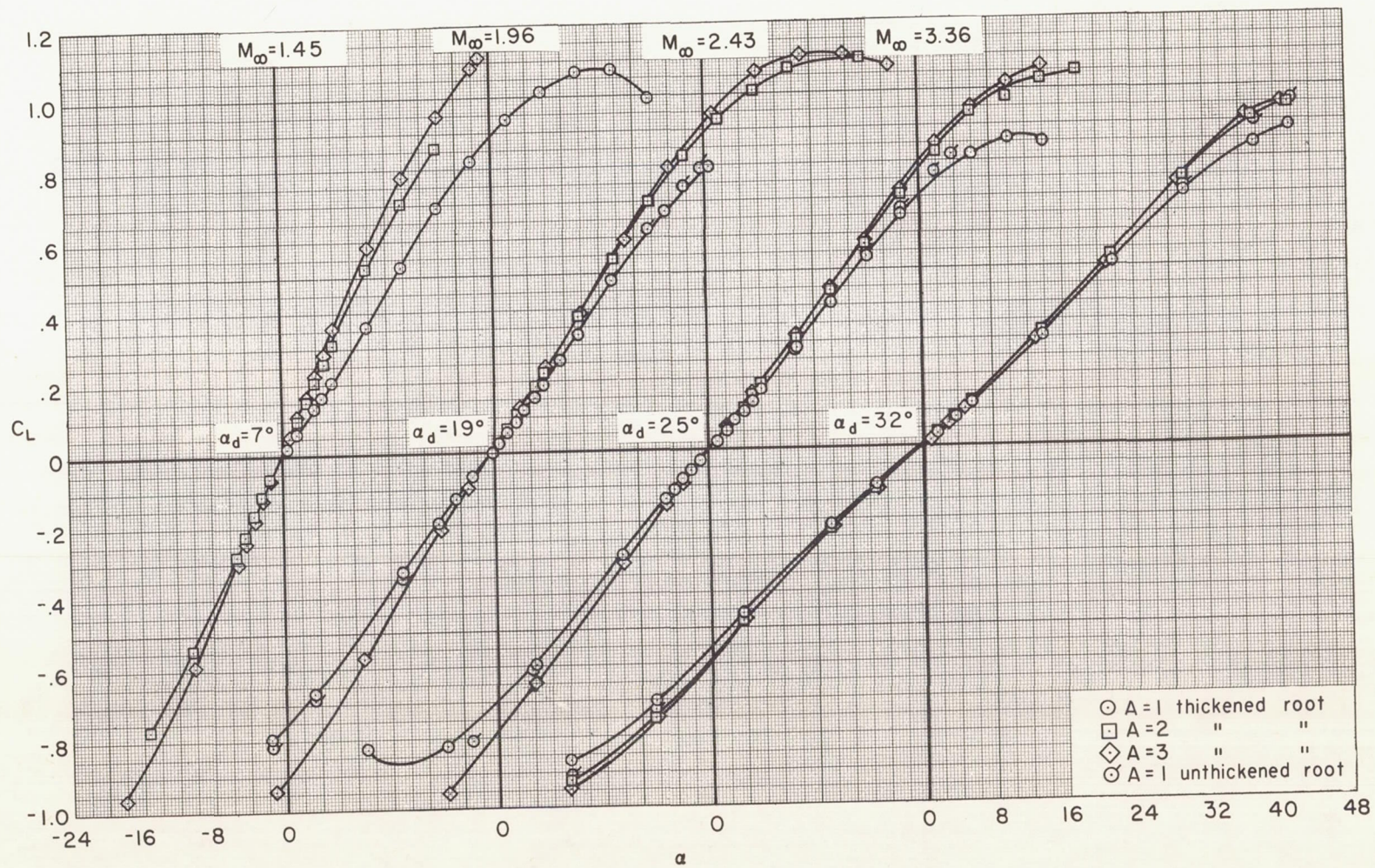
Figure 2.- The effects of Mach number and aspect ratio on the lift coefficient from force tests.
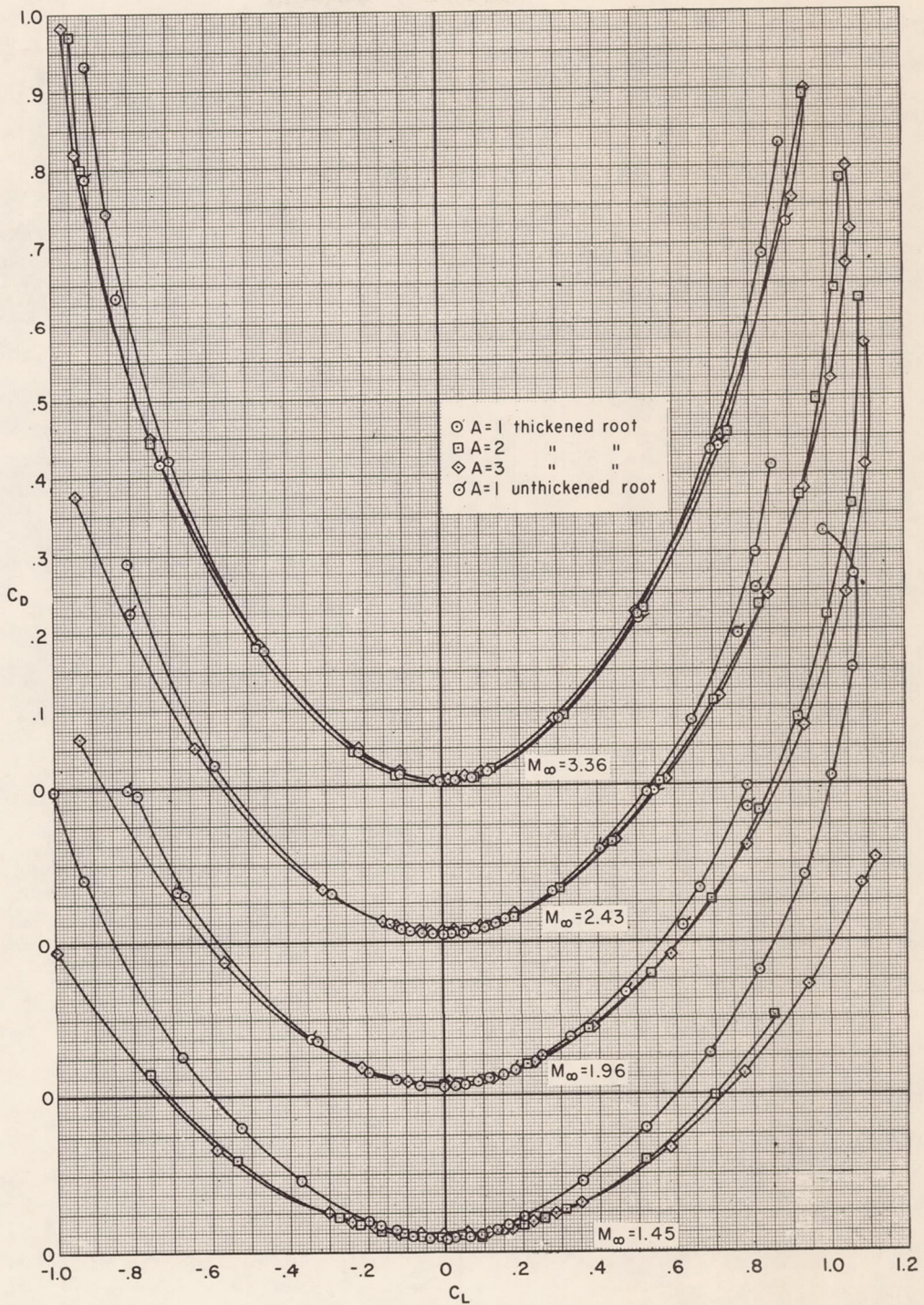
Figure 3.- The effects of Mach number and aspect ratio on the drag
coefficient from force tests.
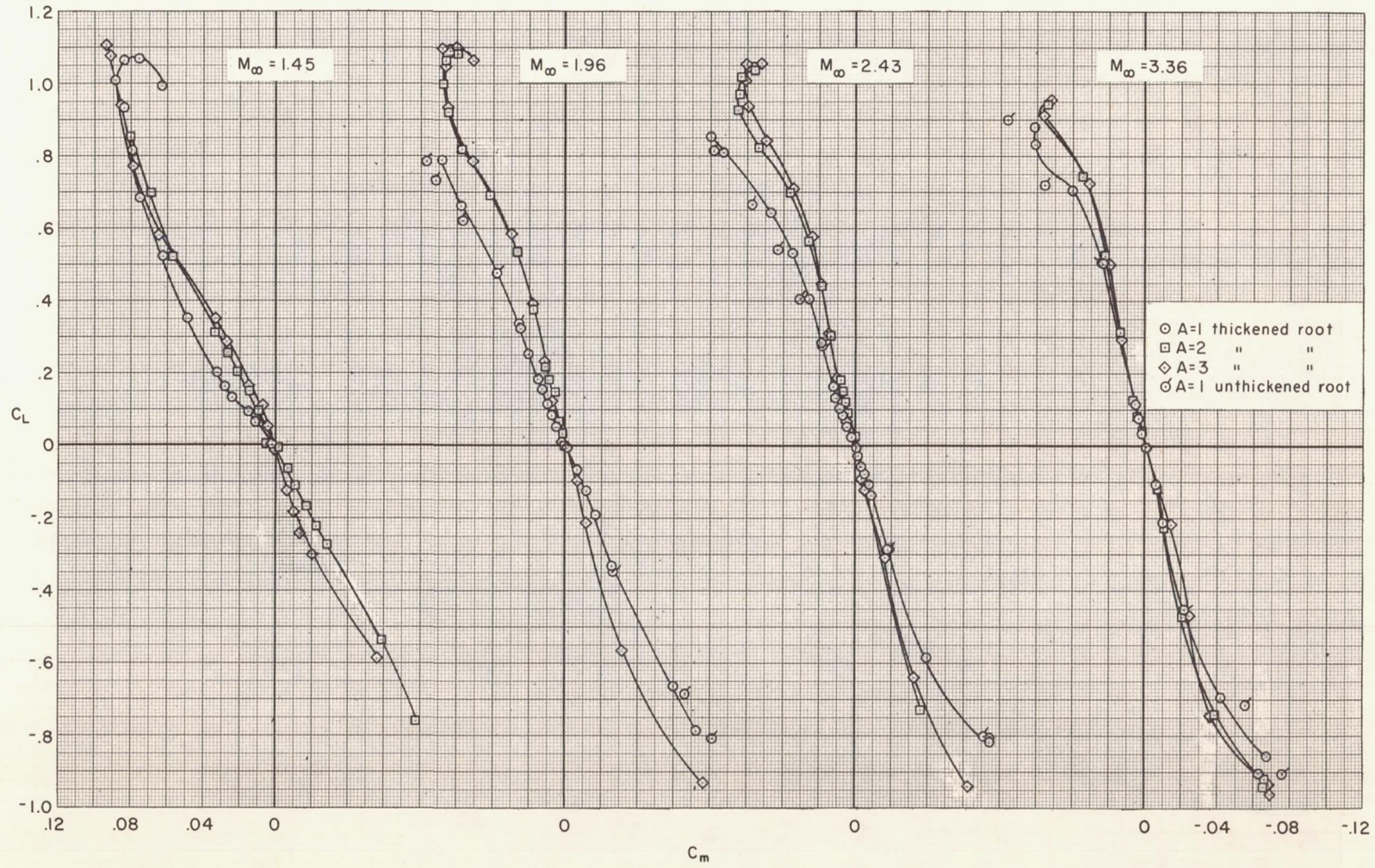
Figure 4.- The effects of Mach number and aspect ratio on the pitching-moment coefficient from force tests.
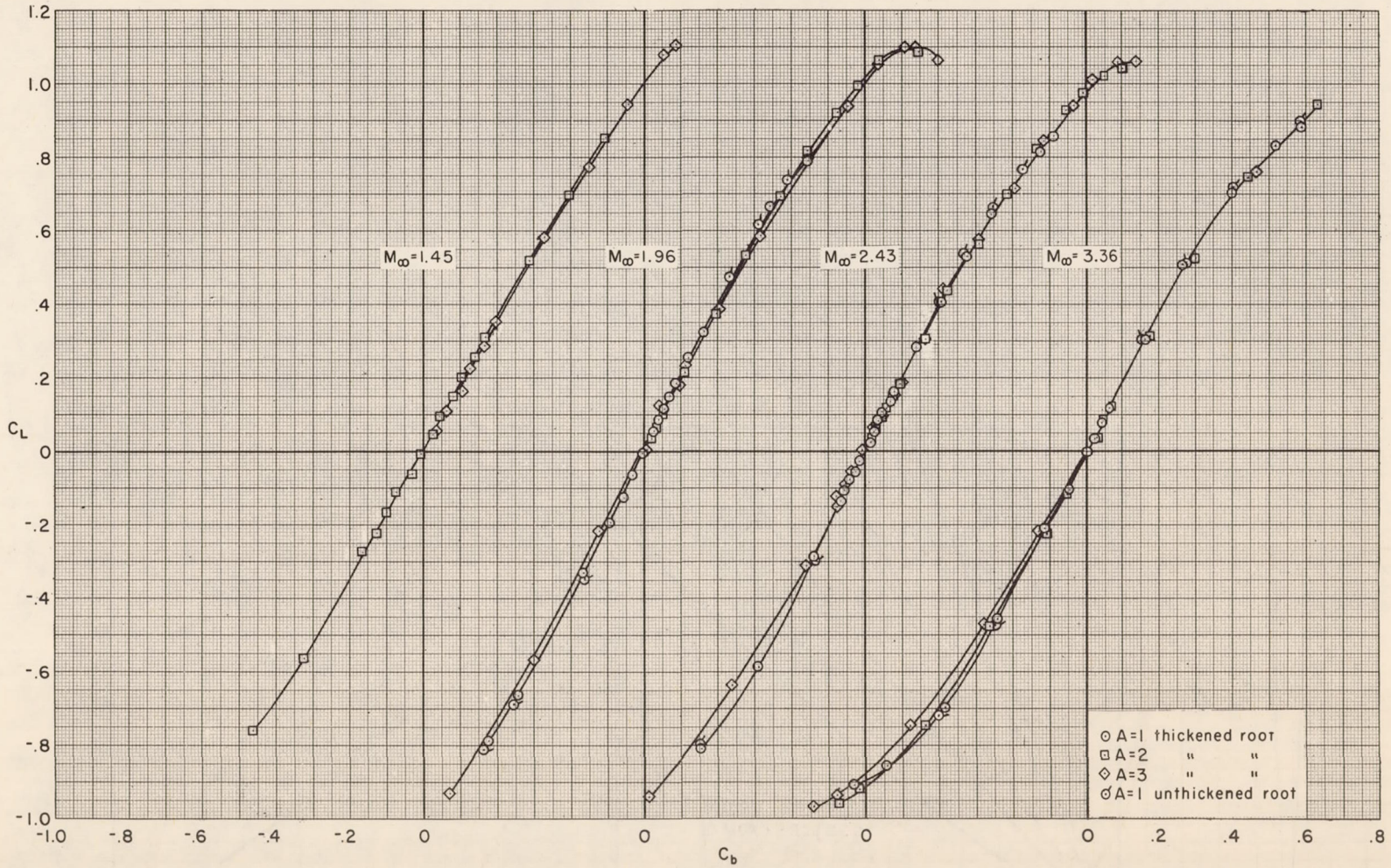
Figure 5.- The effects of Mach number and aspect ratio on the root-bending-moment coefficient from force tests.
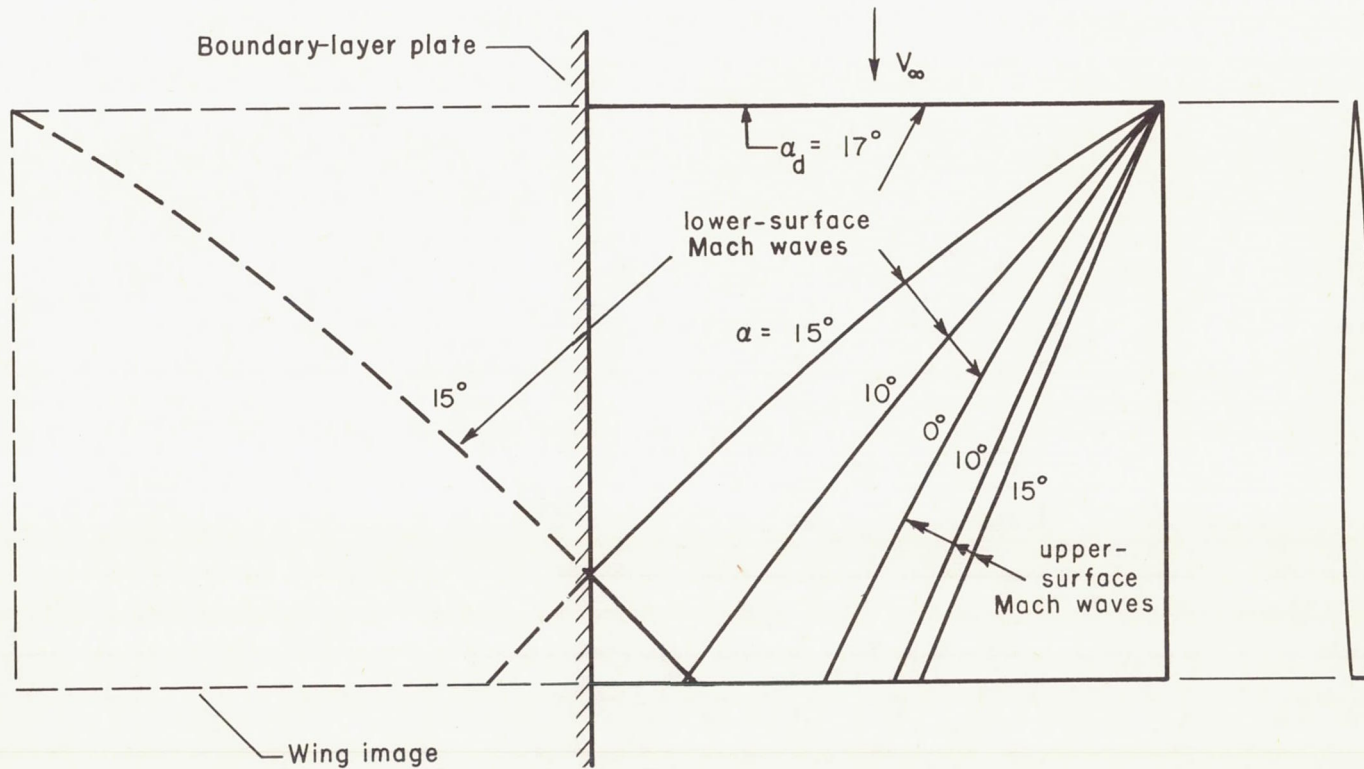
Figure 6.- Tip Mach curves on the pressure-distribution wings as computed by shock-expansion theory; A = 2, M_∞ = 1.97.
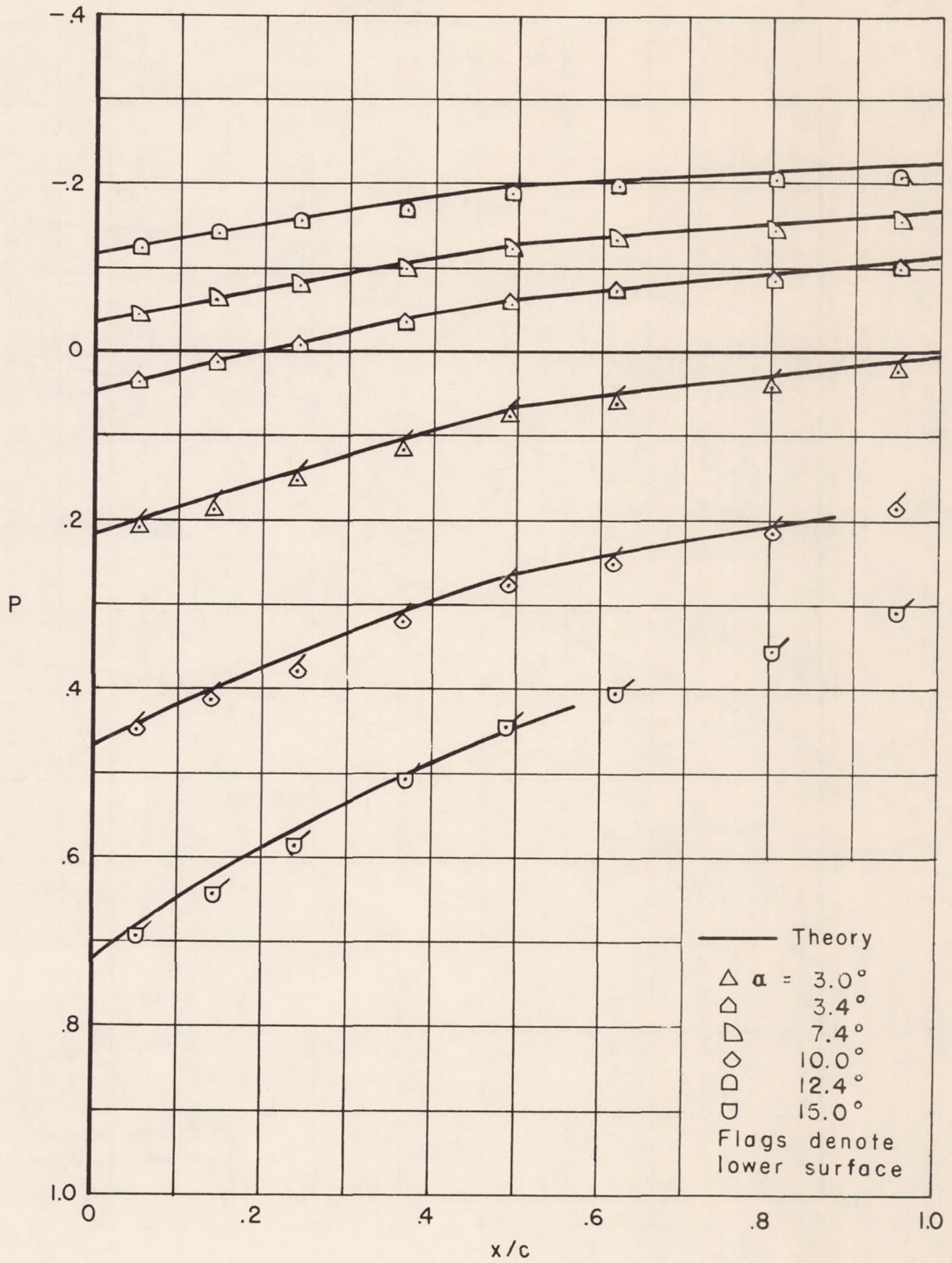
(a) $M_\infty = 1.97$, $y/s = 0.250$

Figure 7.- Comparison between shock-expansion theory and the experimental
pressure distribution on the unthickened root wing.
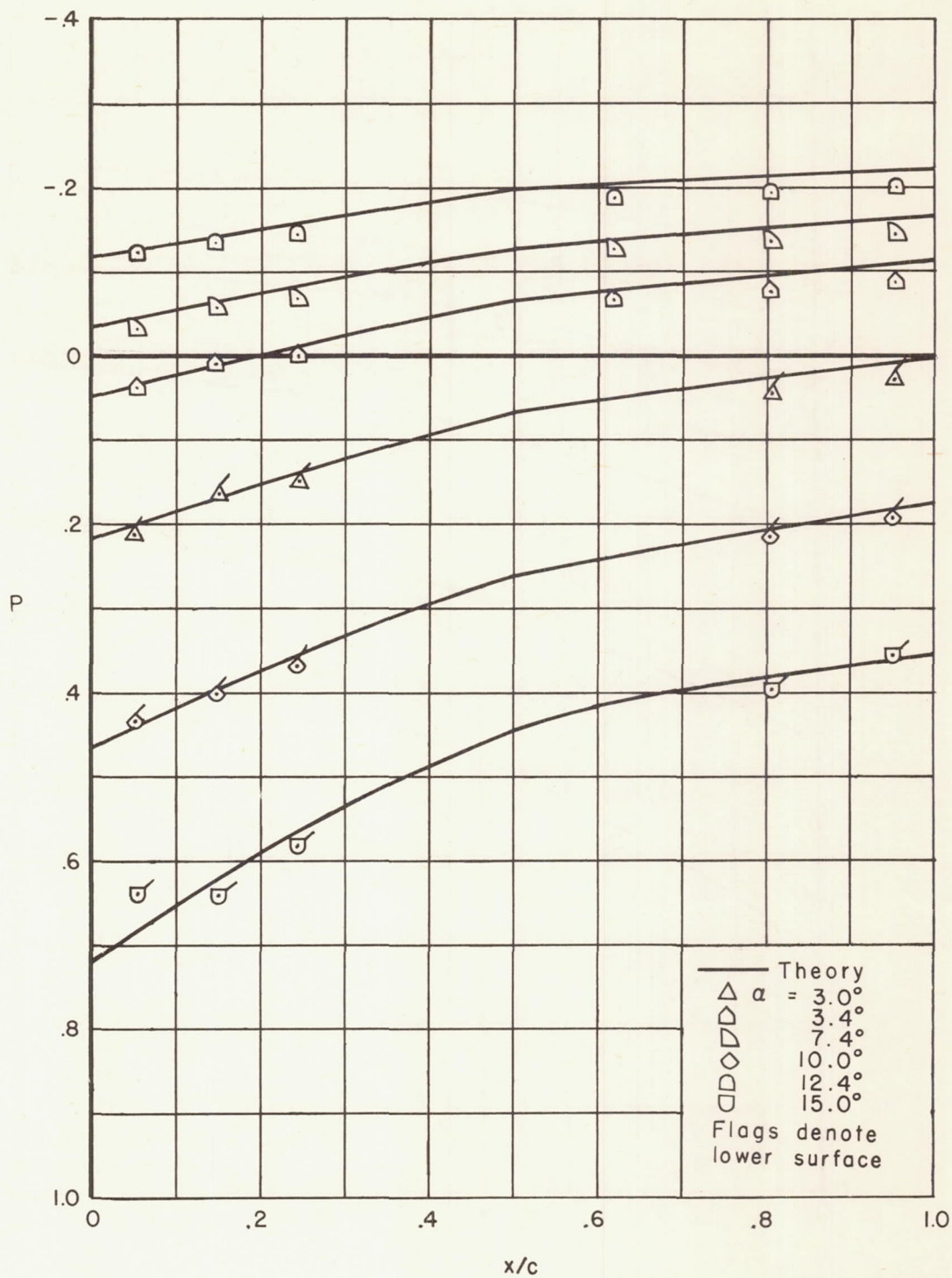
(b) $M_\infty = 1.97$, $y/s = 0.025$

Figure 7.- Continued.
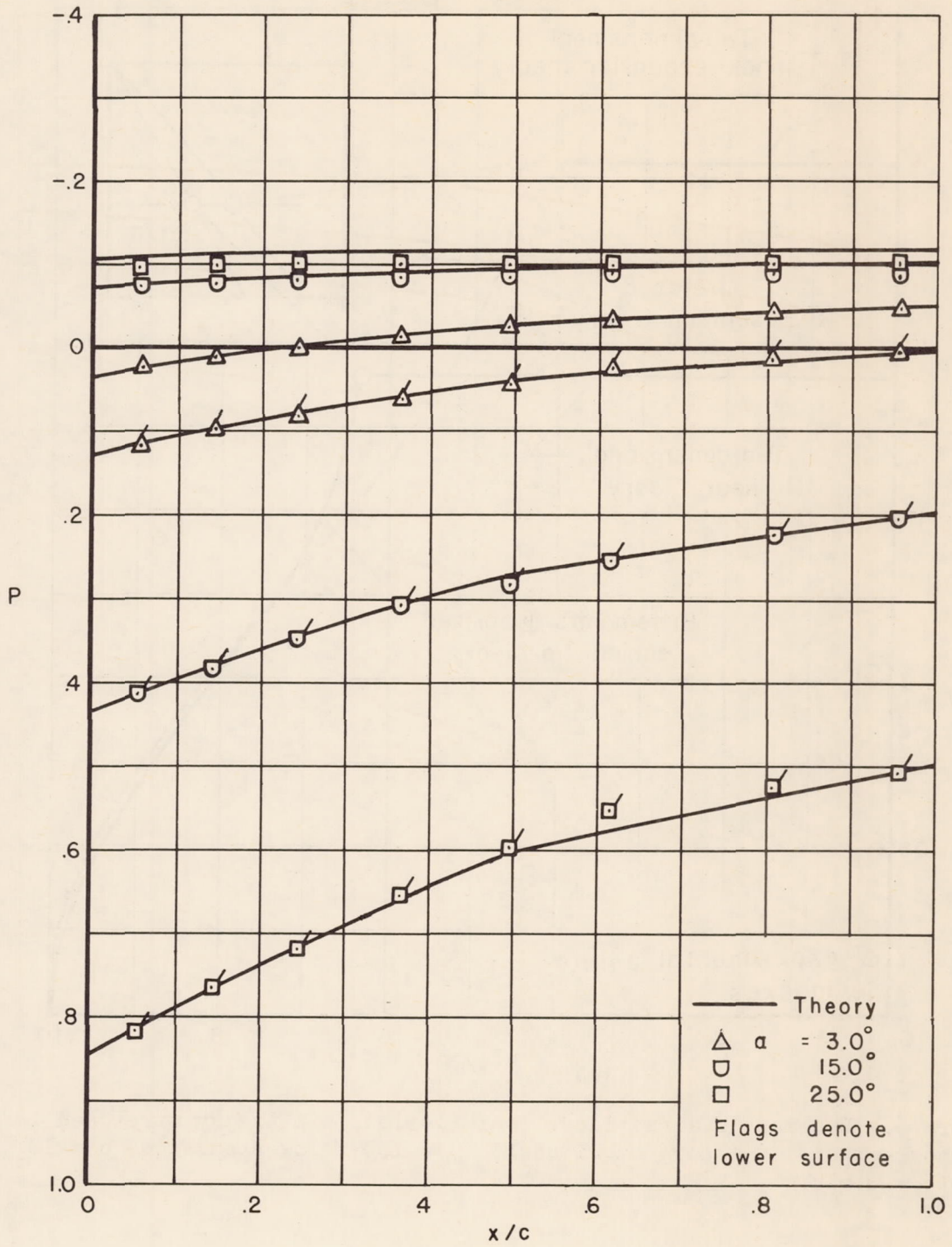
(c) $M_\infty = 3.36$, $y/s = 0.250$

Figure 7.- Concluded.
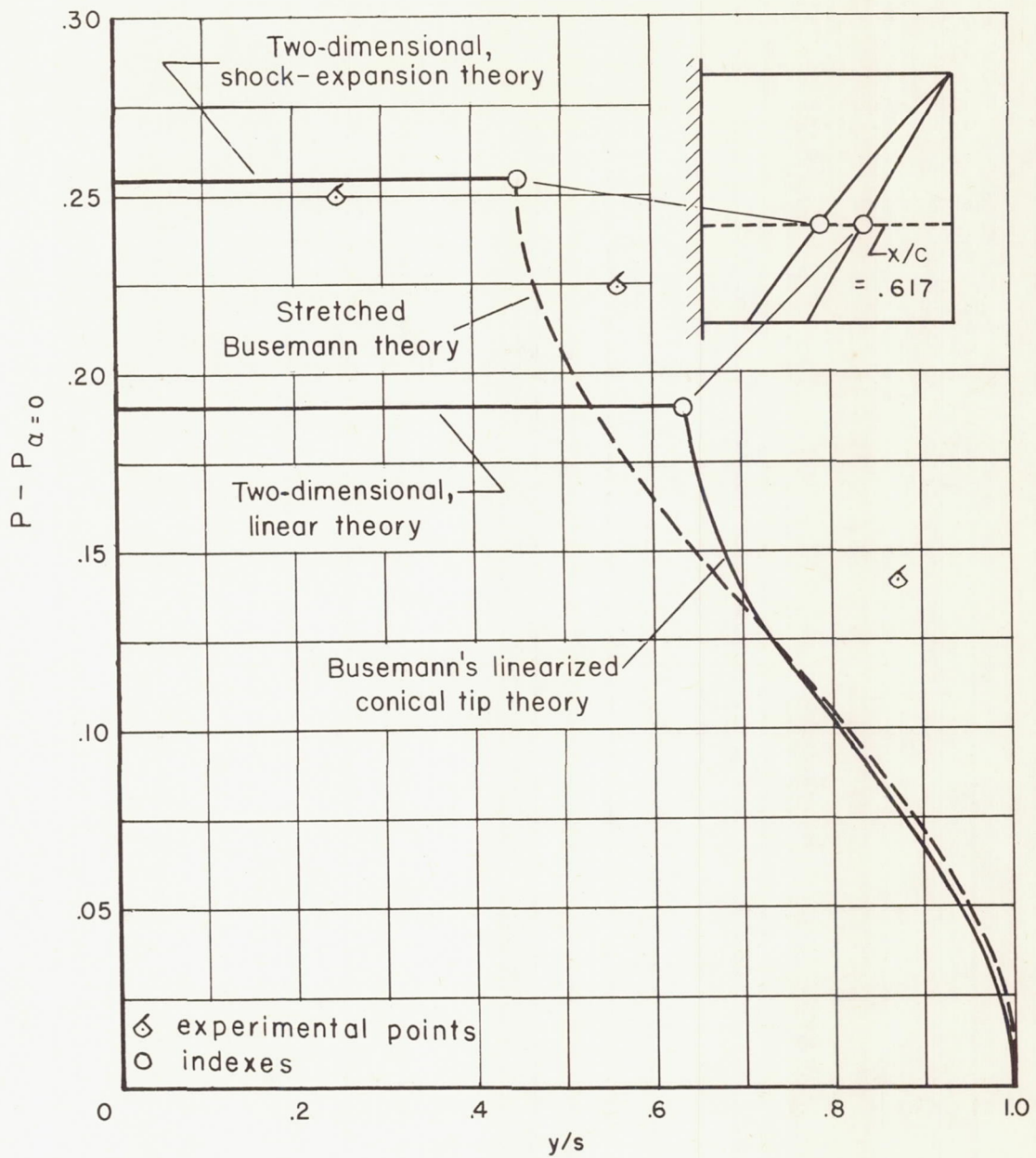
Figure 8.- Busemann's linearized, conical-flow, tip theory stretched to shock-expansion-theory magnitudes; $M_\infty = 1.97$, lower surface, $\alpha = 10^\circ$, $x/c = 0.617$.
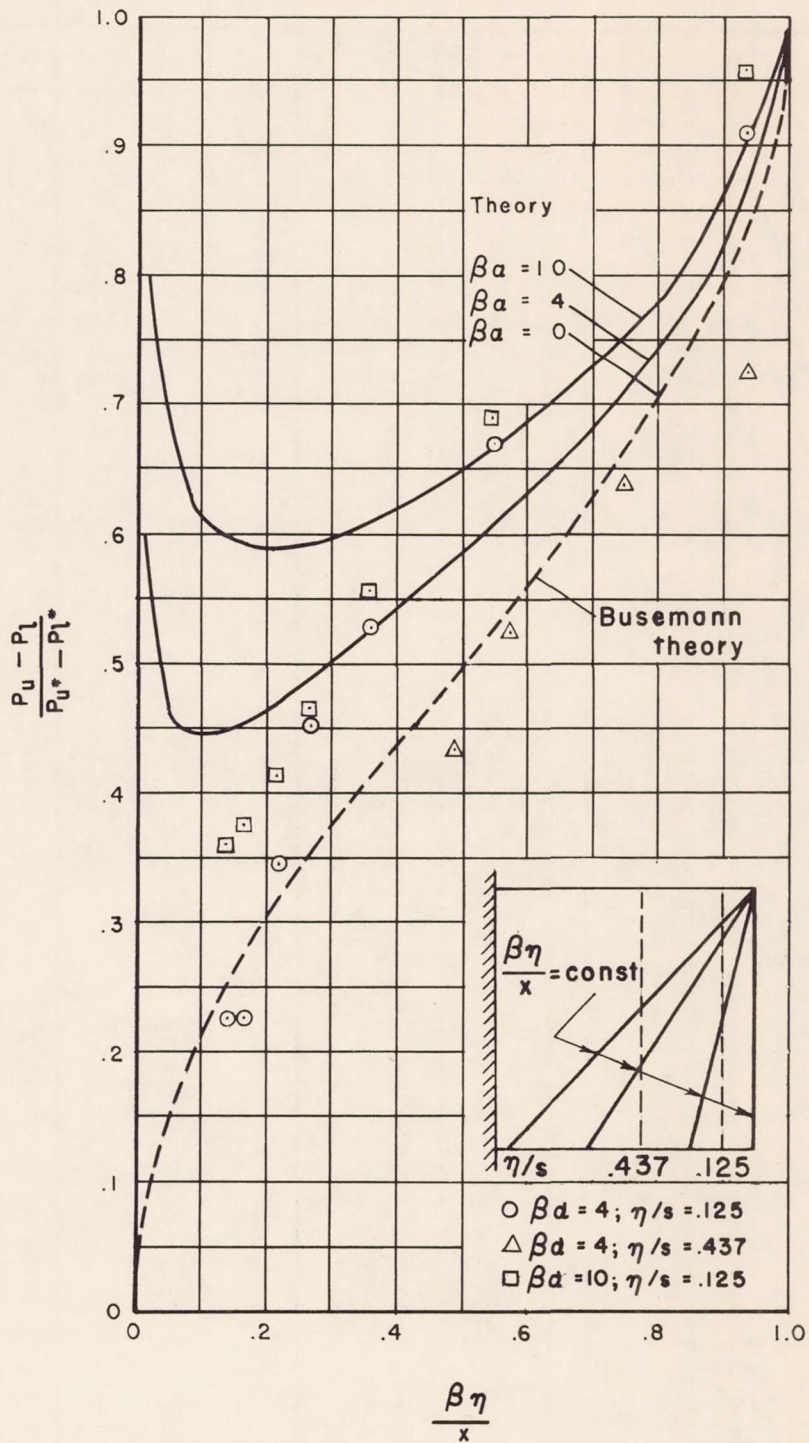
Figure 9.- Experimental tip loading and linearized theory of
reference 13; $M_\infty = 1.45$.
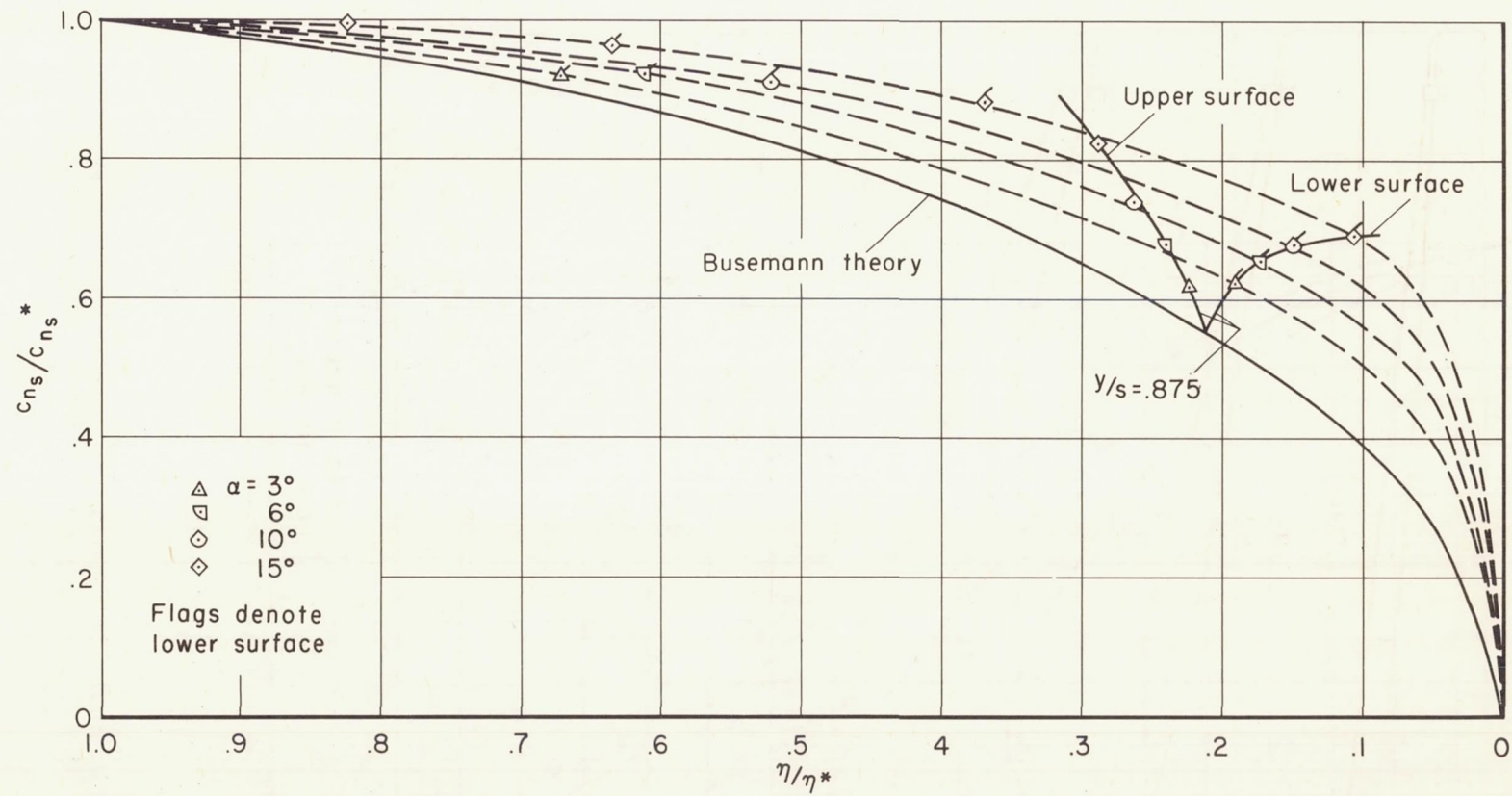
Figure 10.- Variation of normalized, single-surface span loading with angle of attack in the tip region of the rectangular pressure distribution wing; $M_\infty = 1.97$.

$$\left\{ \begin{array}{l} \left(c_{n_s}/c_{n_s}^*\right)_u = \left(c_{n_s}/c_{n_s}^*\right)_B + k_u \beta^{-1/3} \alpha \\ \left(c_{n_s}/c_{n_s}^*\right)_l = \left(c_{n_s}/c_{n_s}^*\right)_B + k_l \beta^{3/2} \alpha^{1/\beta} \end{array} \right.$$

⊙ Buseman's theory
▫ Upper surface
◩ Lower surface
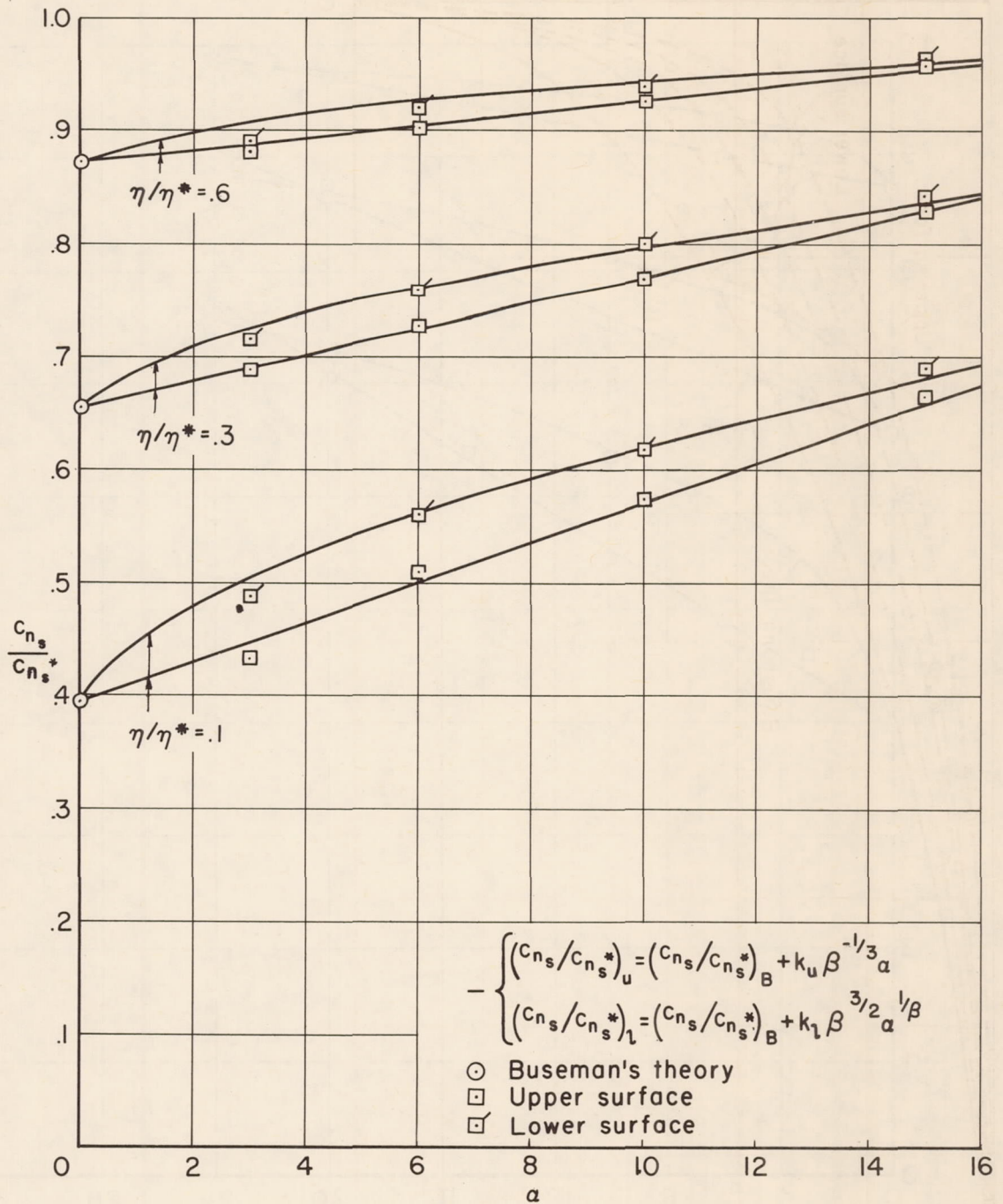
(a) $M_\infty = 1.97$

Figure 11.- Variation of $c_{n_s}/c_{n_s}^*$ for fixed values of η/η^*.
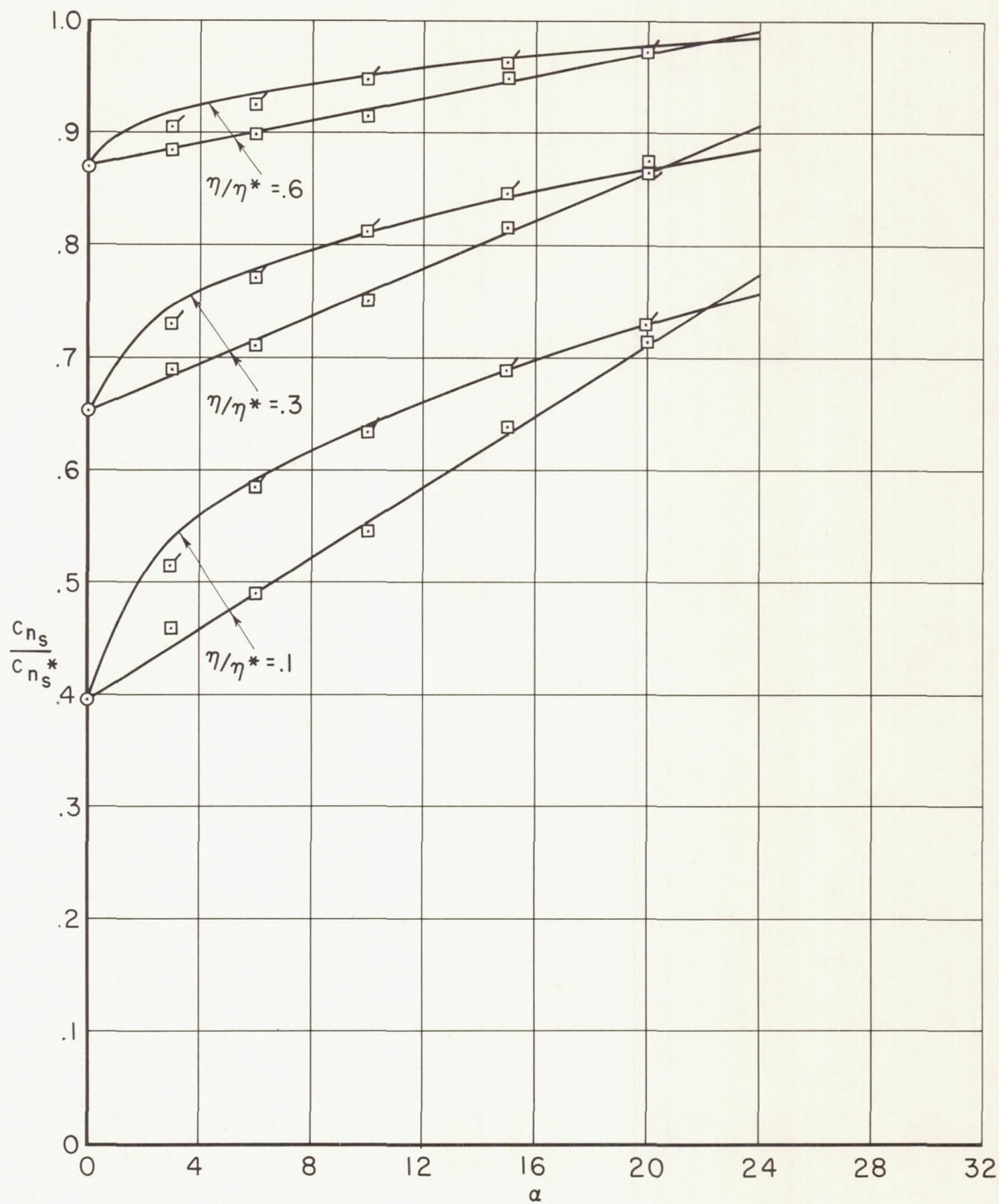
(b) $M_\infty = 2.46$

Figure 11.- Continued.
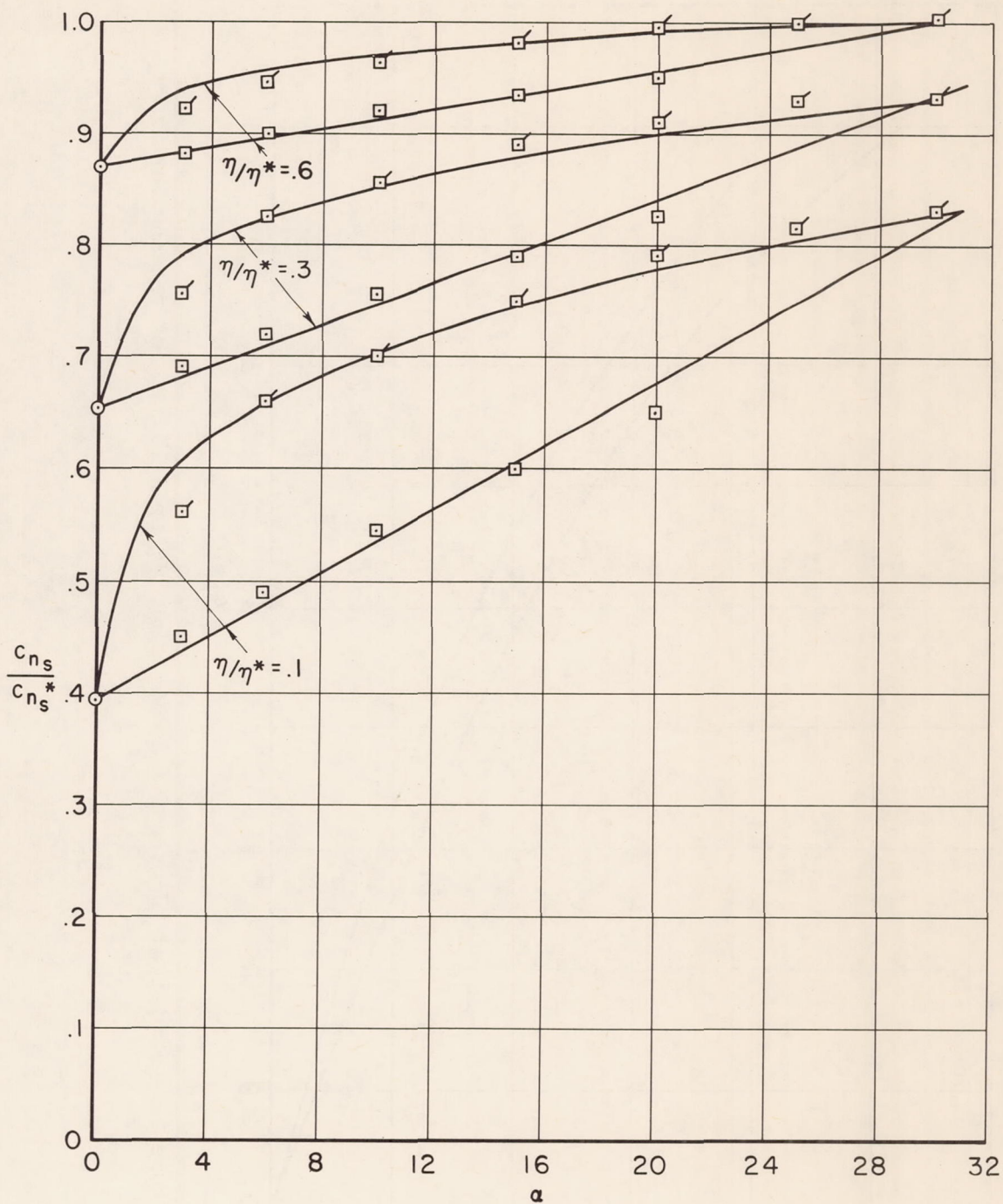
(c) $M_\infty = 3.36$

Figure 11.- Concluded.
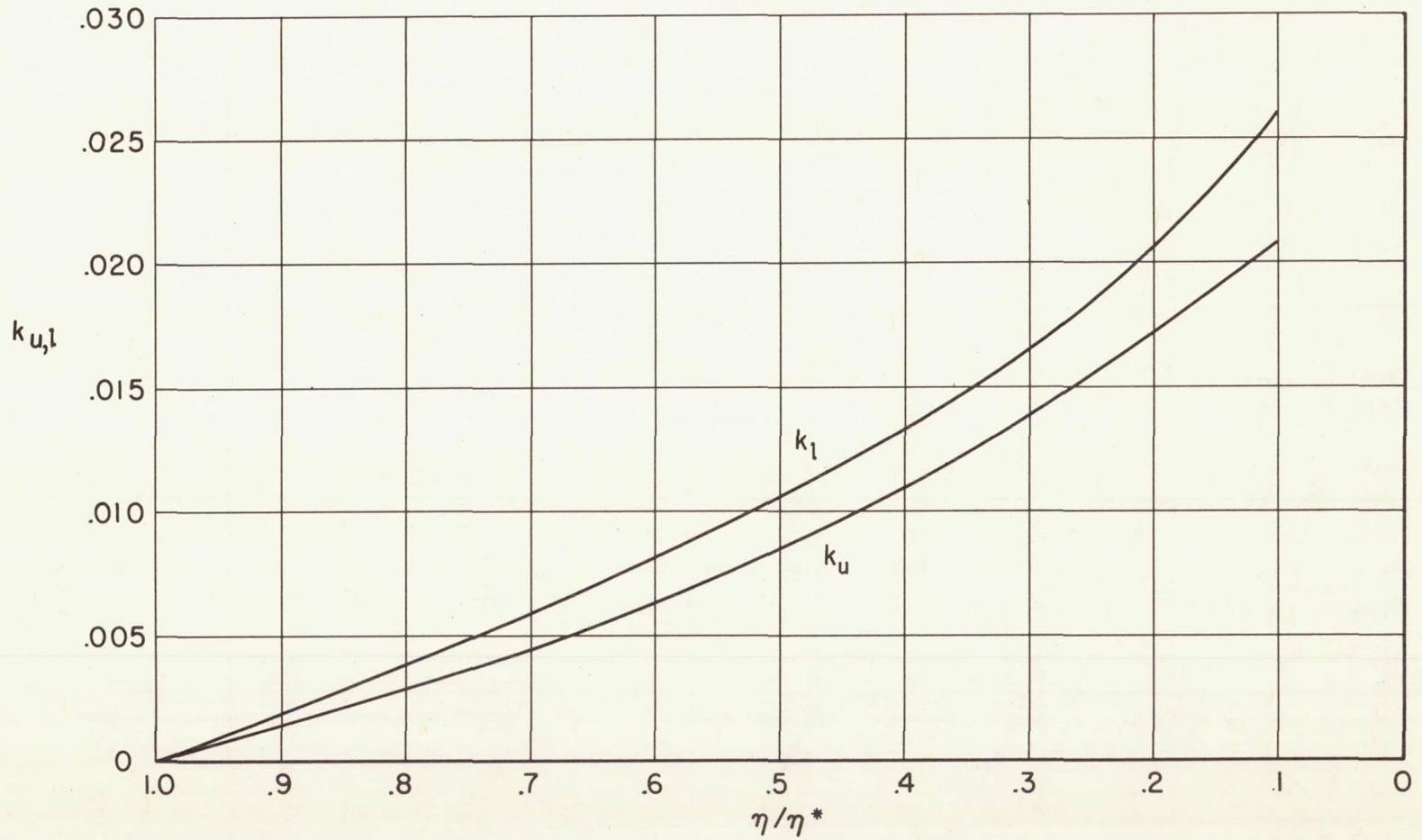
Figure 12.- Empirical factors for determining tip span loading of rectangular wings.
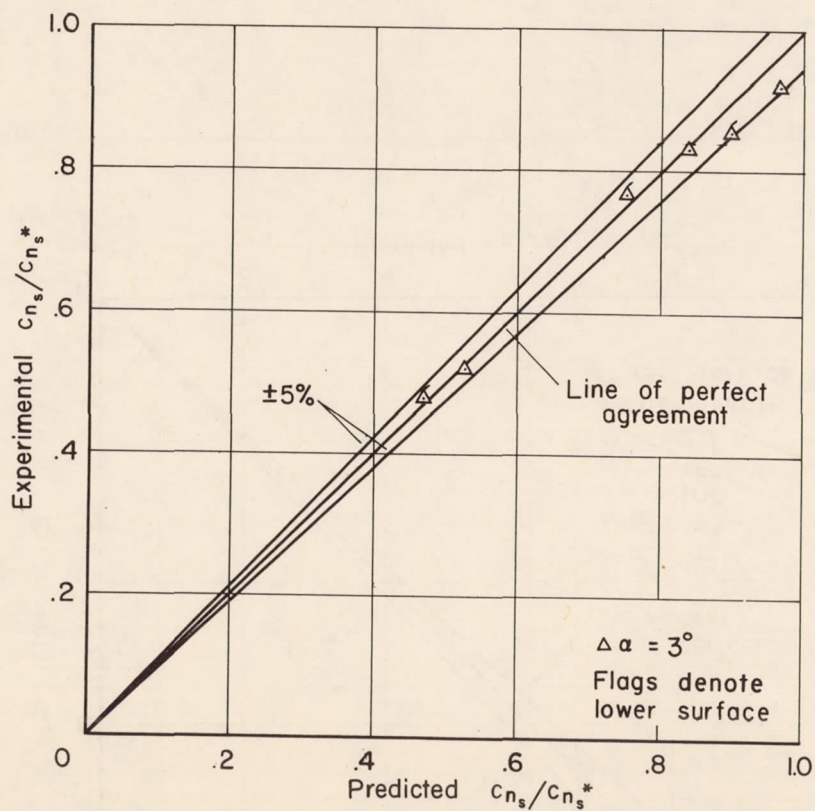
(a) $M_\infty = 1.45$
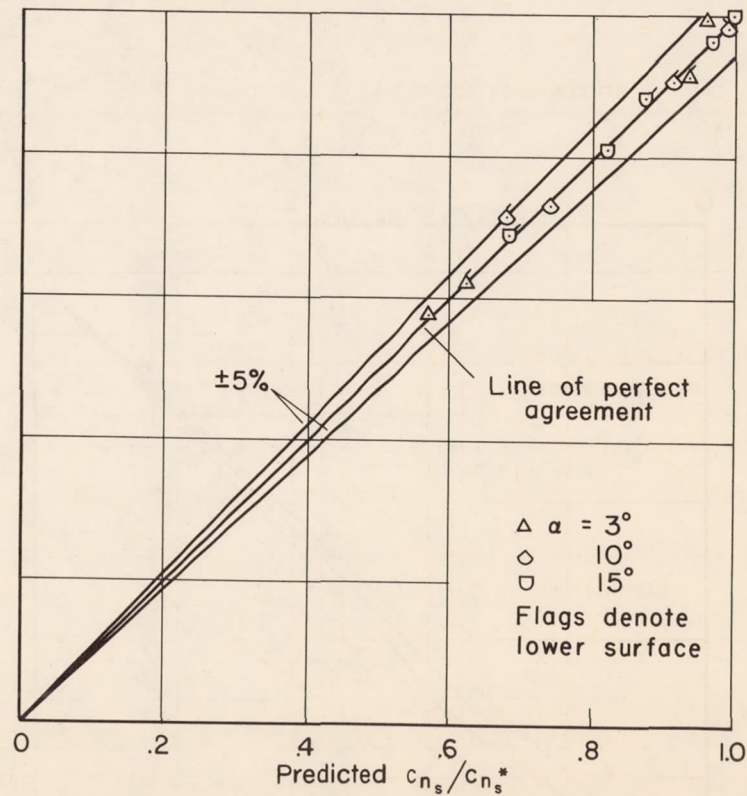
(b) $M_\infty = 1.97$

Figure 13.— Correlation between experimental and predicted values of $c_{n_s}/c_{n_s}*$ in the tip region of the rectangular wing.
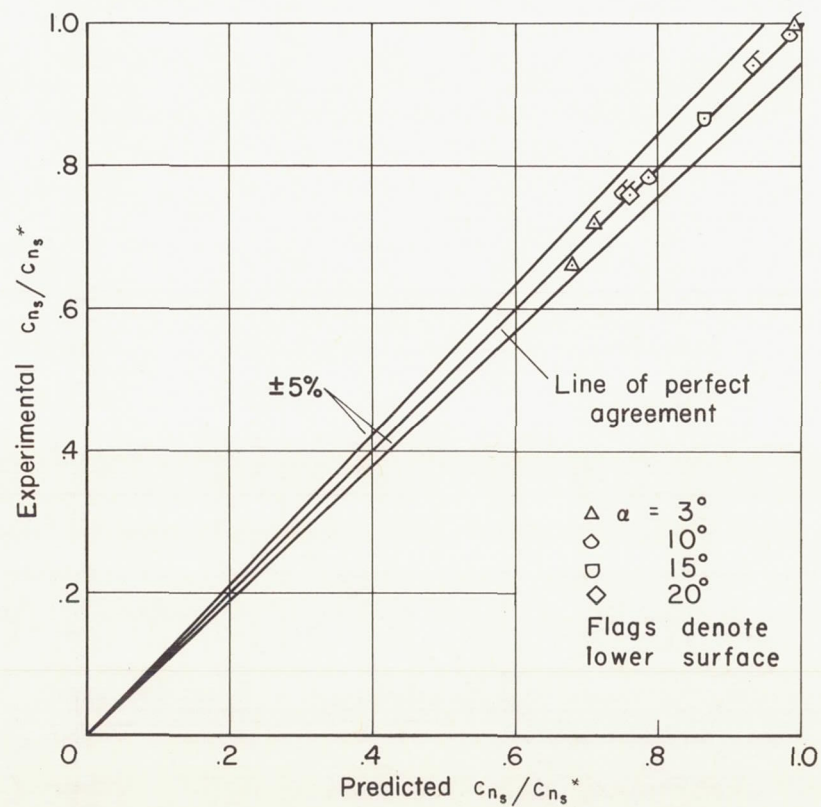
(c) $M_\infty = 2.46$
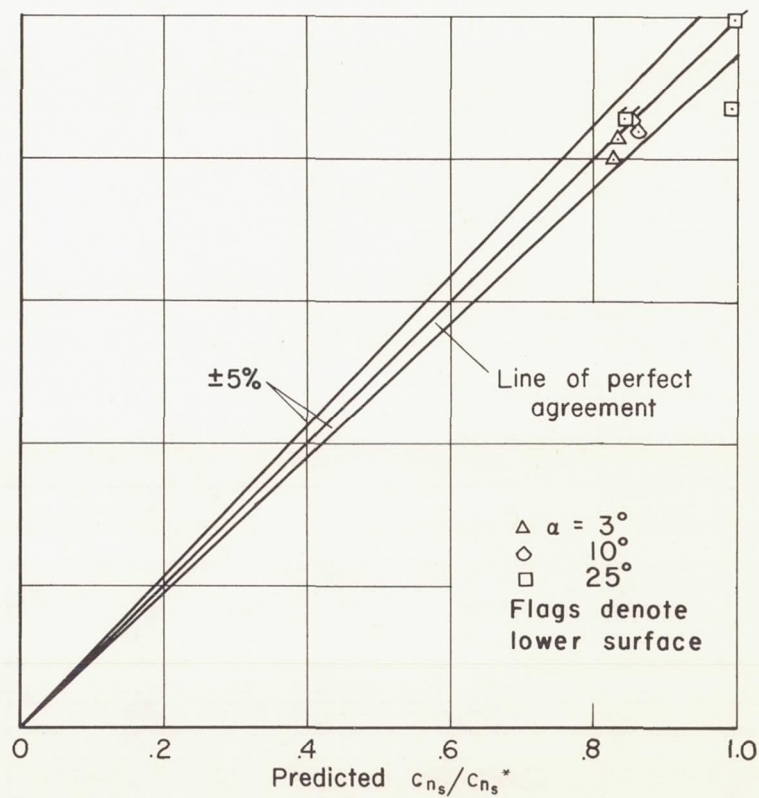
(d) $M_\infty = 3.36$

Figure 13.- Concluded.
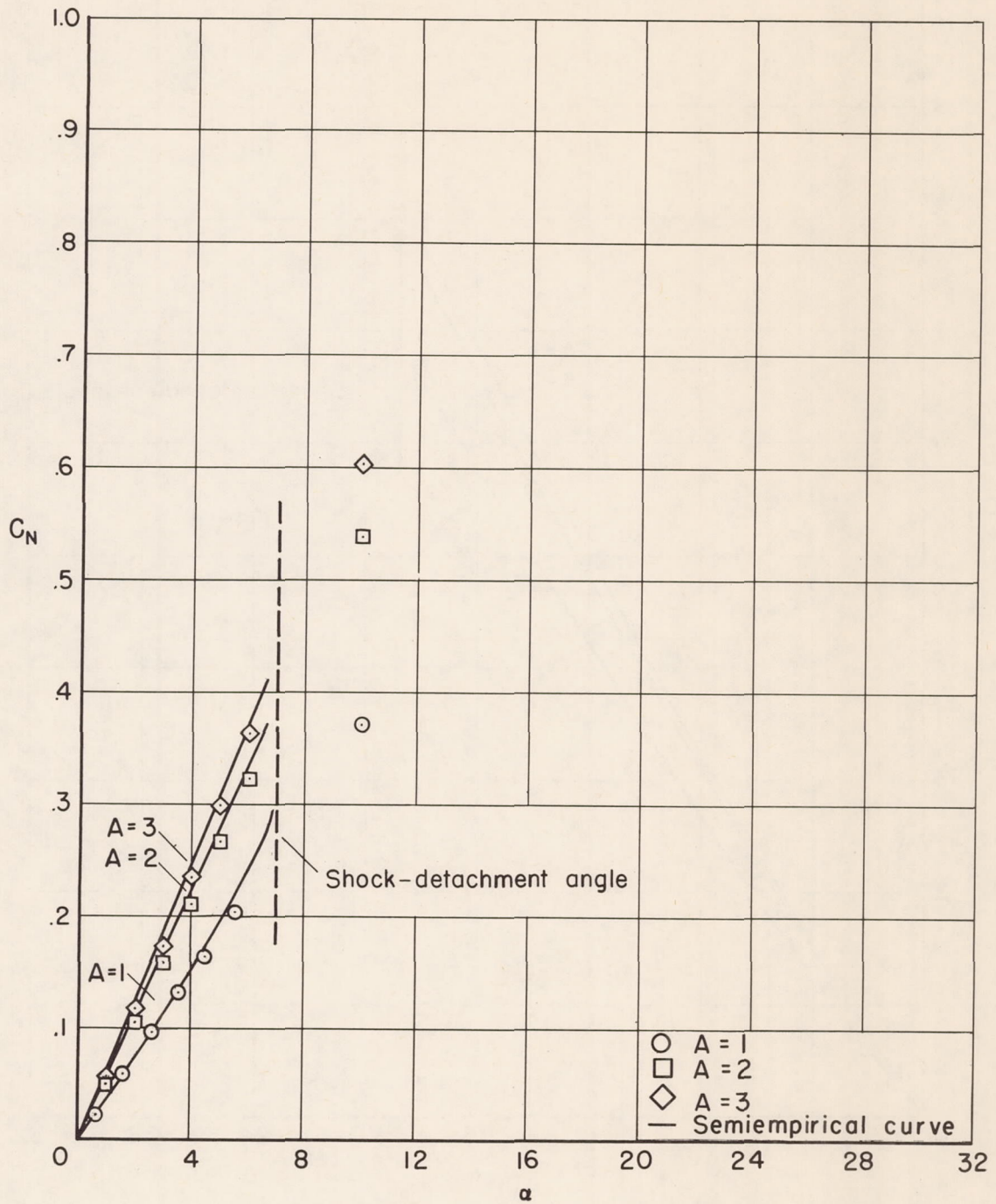
(a) $M_\infty = 1.45$

Figure 14.- Comparison of semiempirical values of C_N with force data.
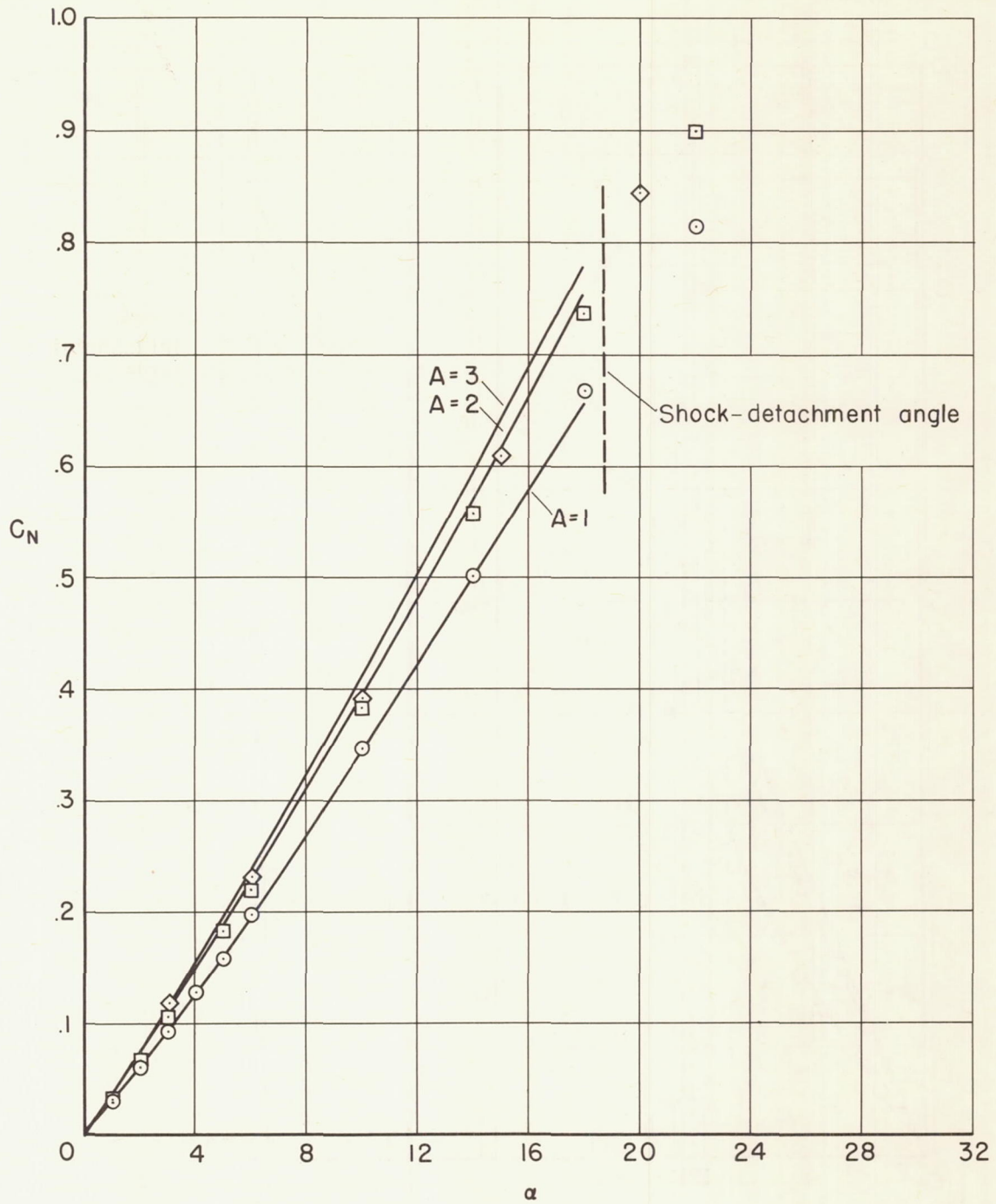
(b) $M_\infty = 1.96$

Figure 14.- Continued.
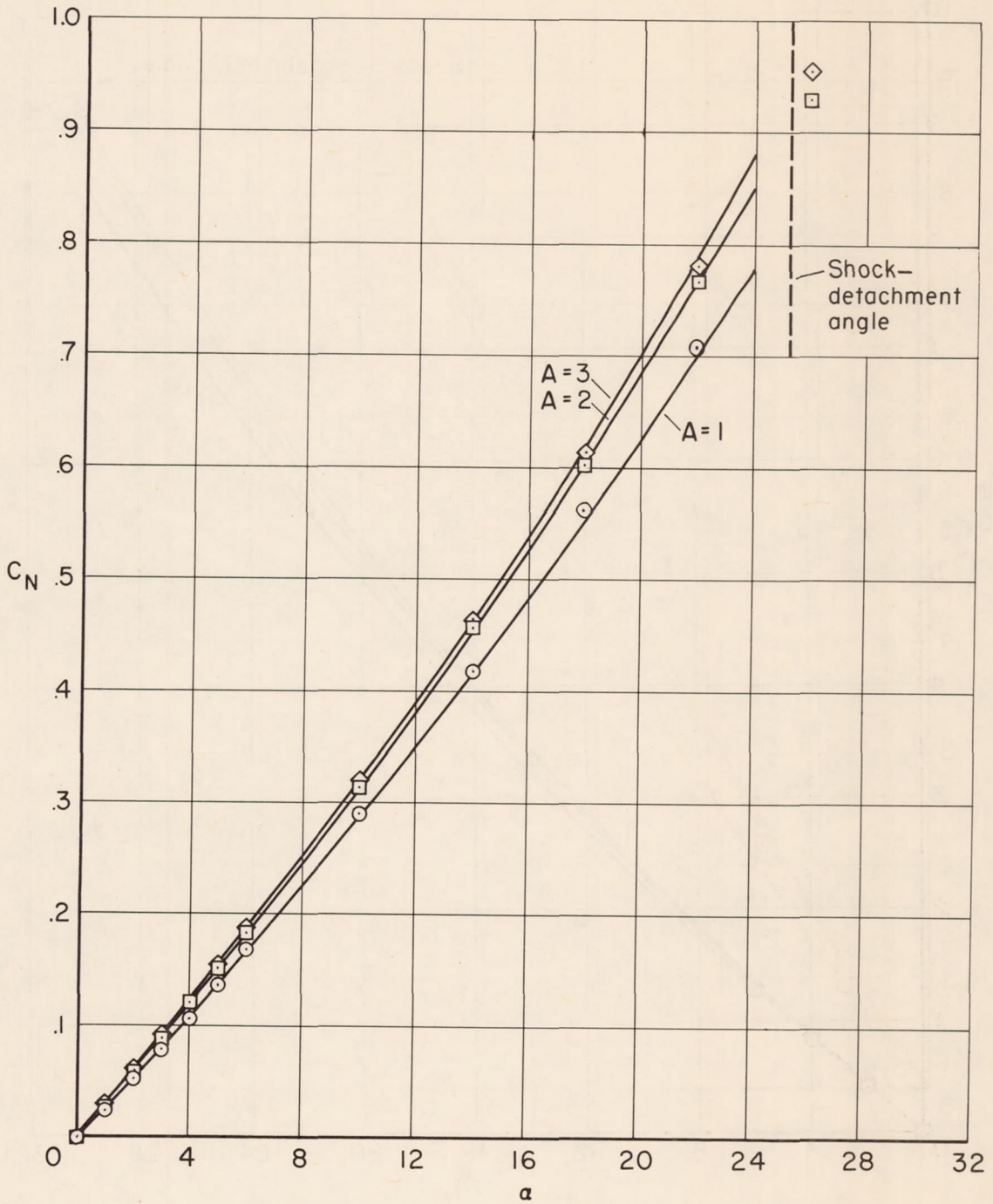
(c) $M_\infty = 2.43$

Figure 14.- Continued.
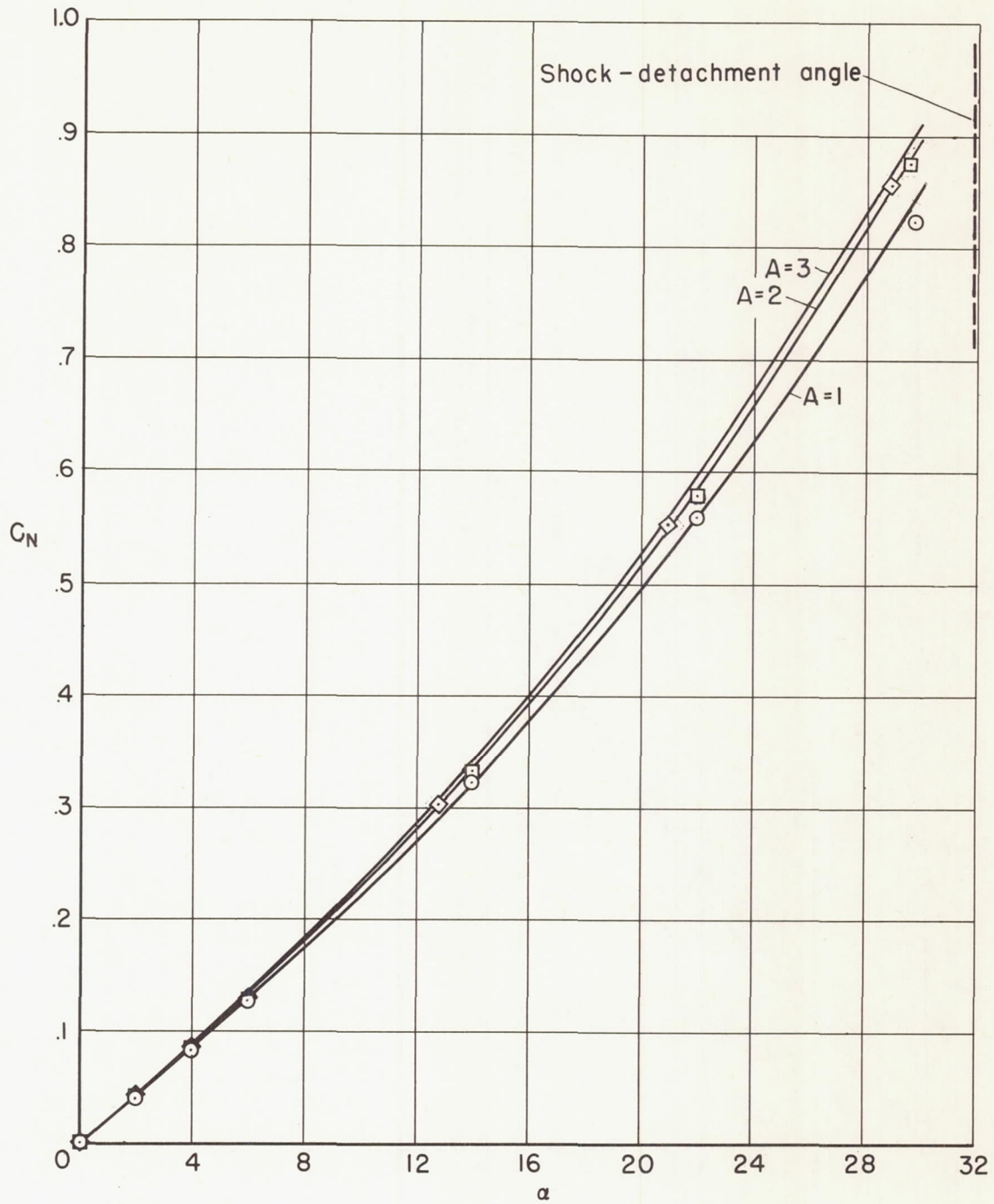
(d) $M_\infty = 3.36$

Figure 14.- Concluded.
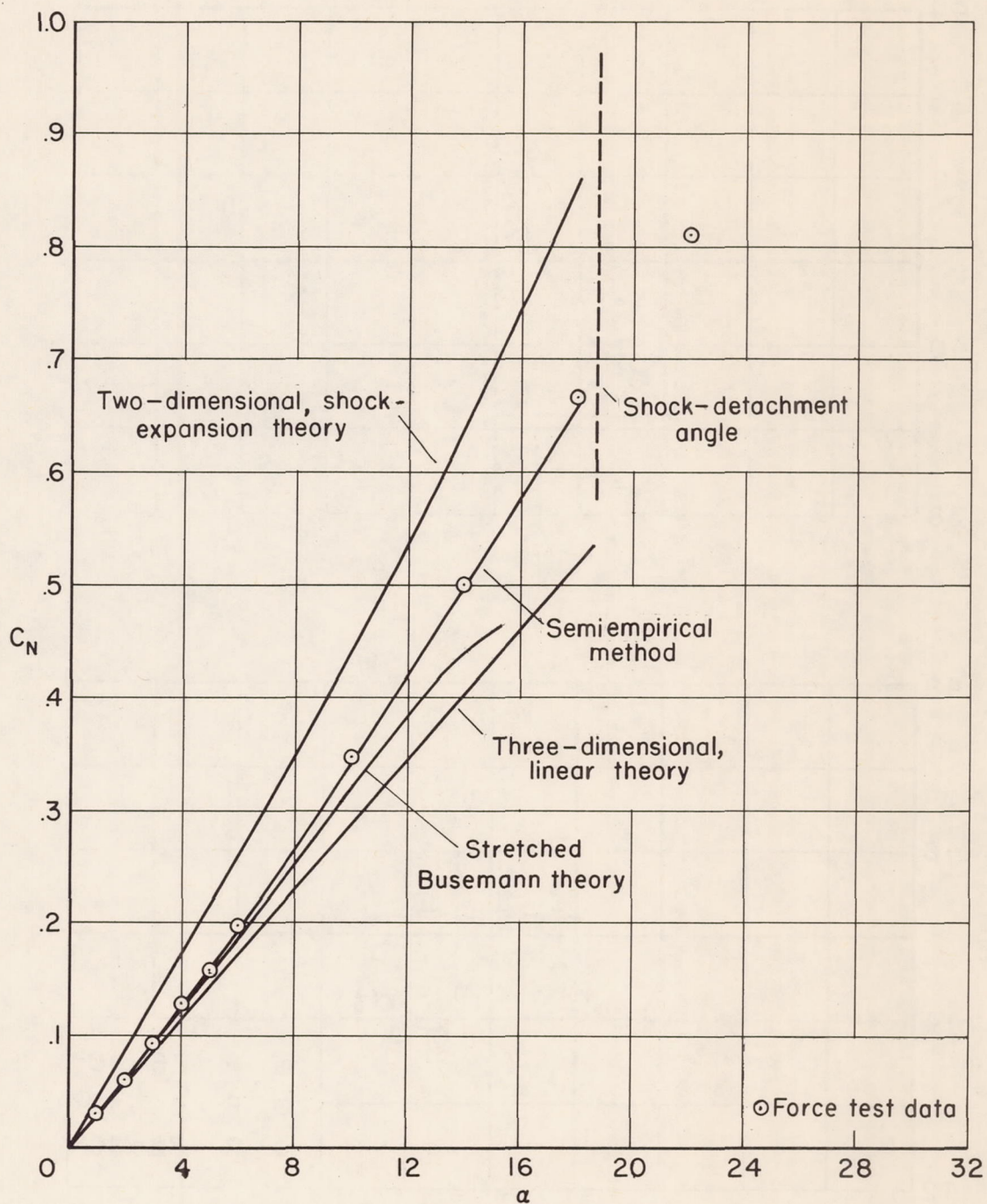
Figure 15.- Comparison of several methods for predicting C_N for $M_\infty = 1.97$; $A = 1$.
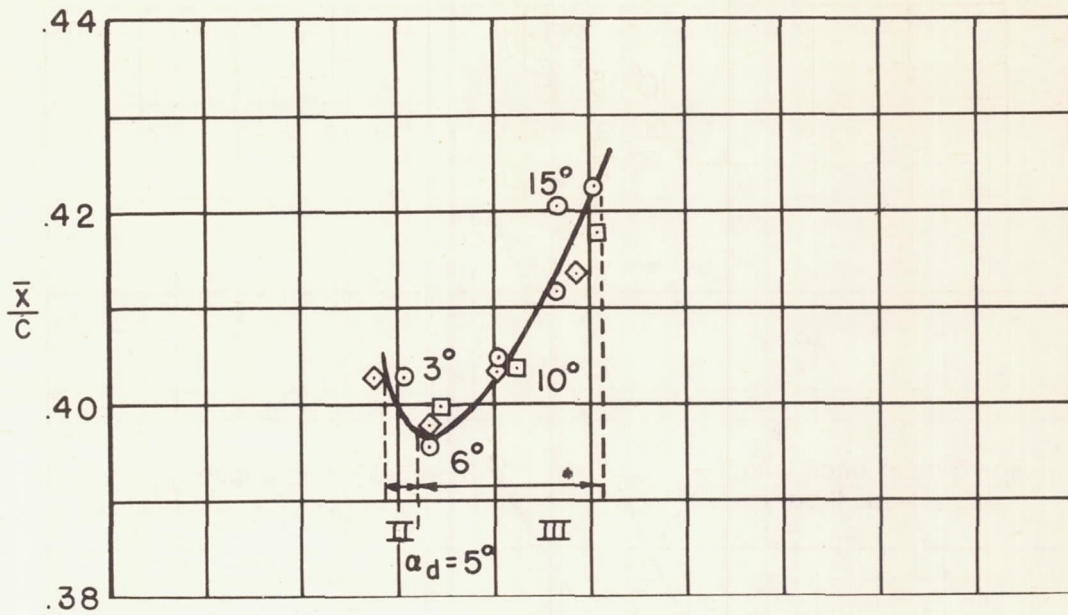
(a) $M_\infty = 1.45$
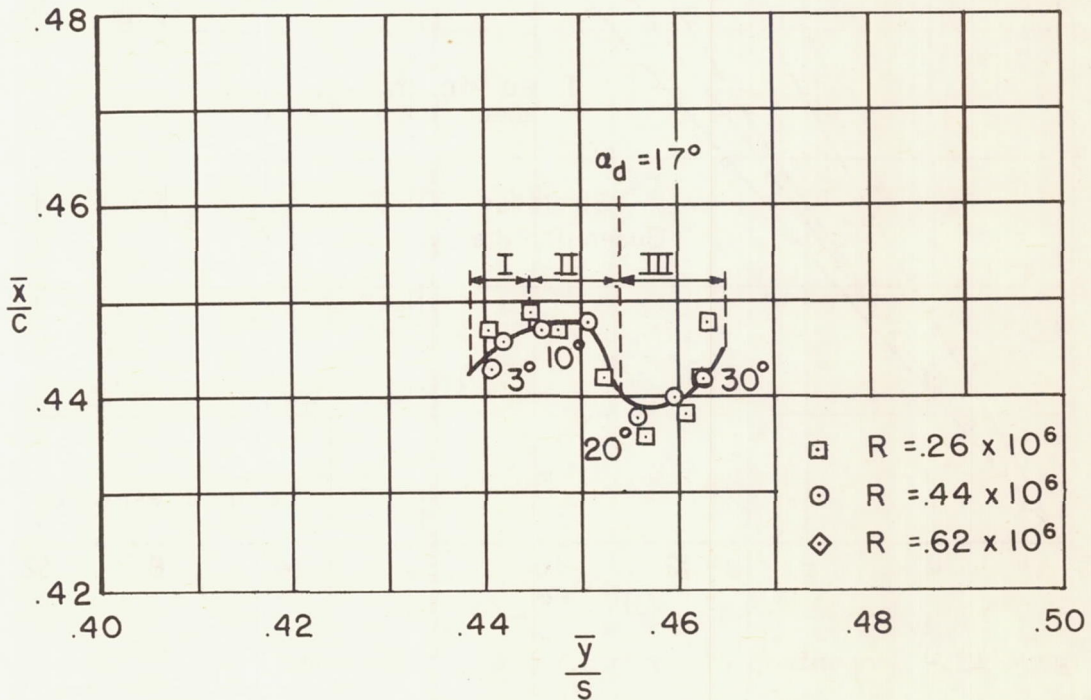
(b) $M_\infty = 1.97$

Figure 16.- Center-of-pressure position from pressure measurements; A = 2.
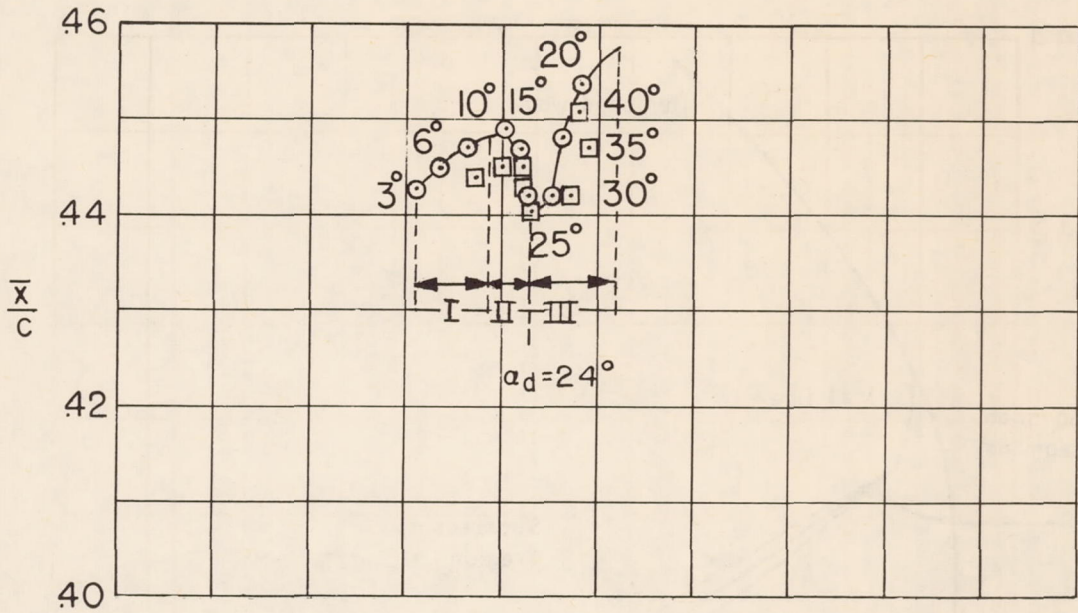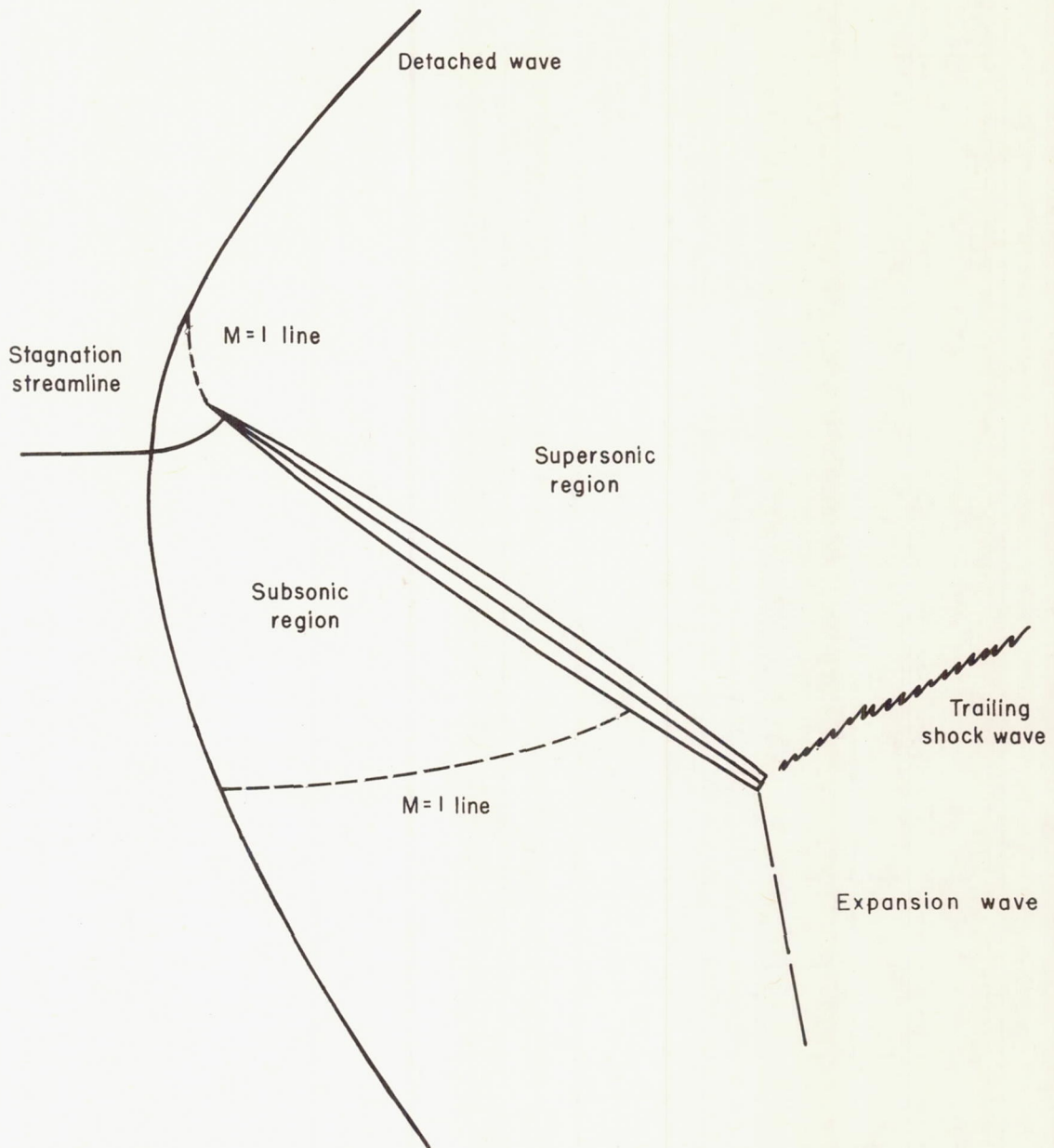
(c) $M_\infty = 2.46$
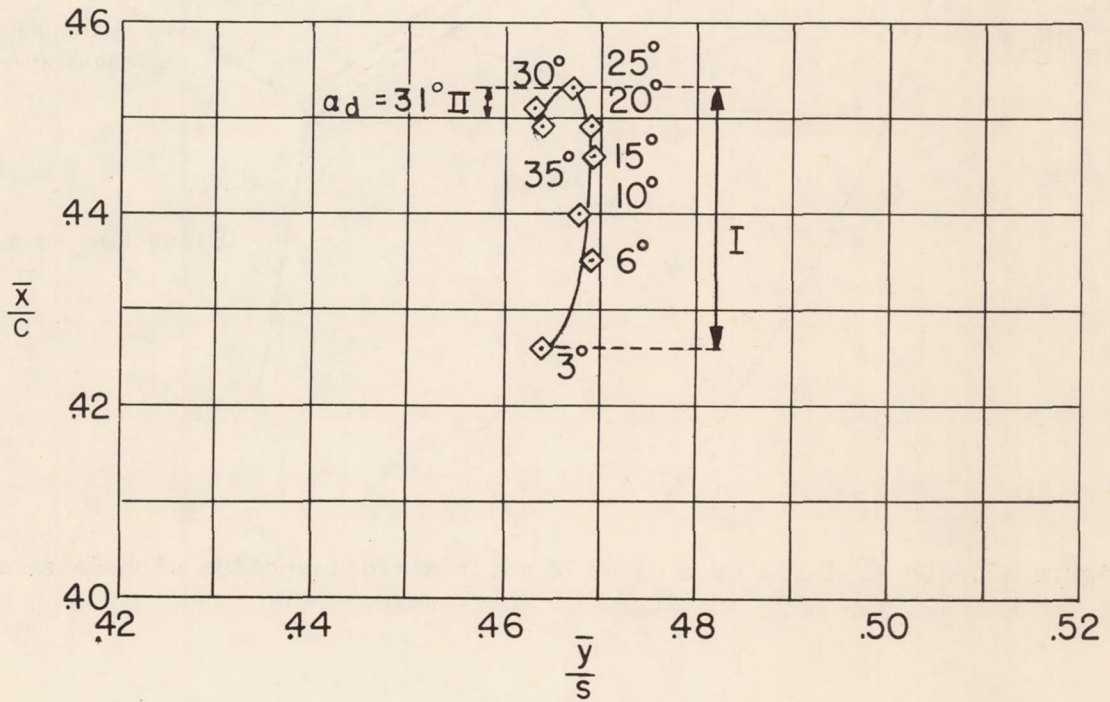
(d) $M_\infty = 3.36$

Figure 16.- Concluded.

Figure 17.- General features of flow about airfoil section with detached
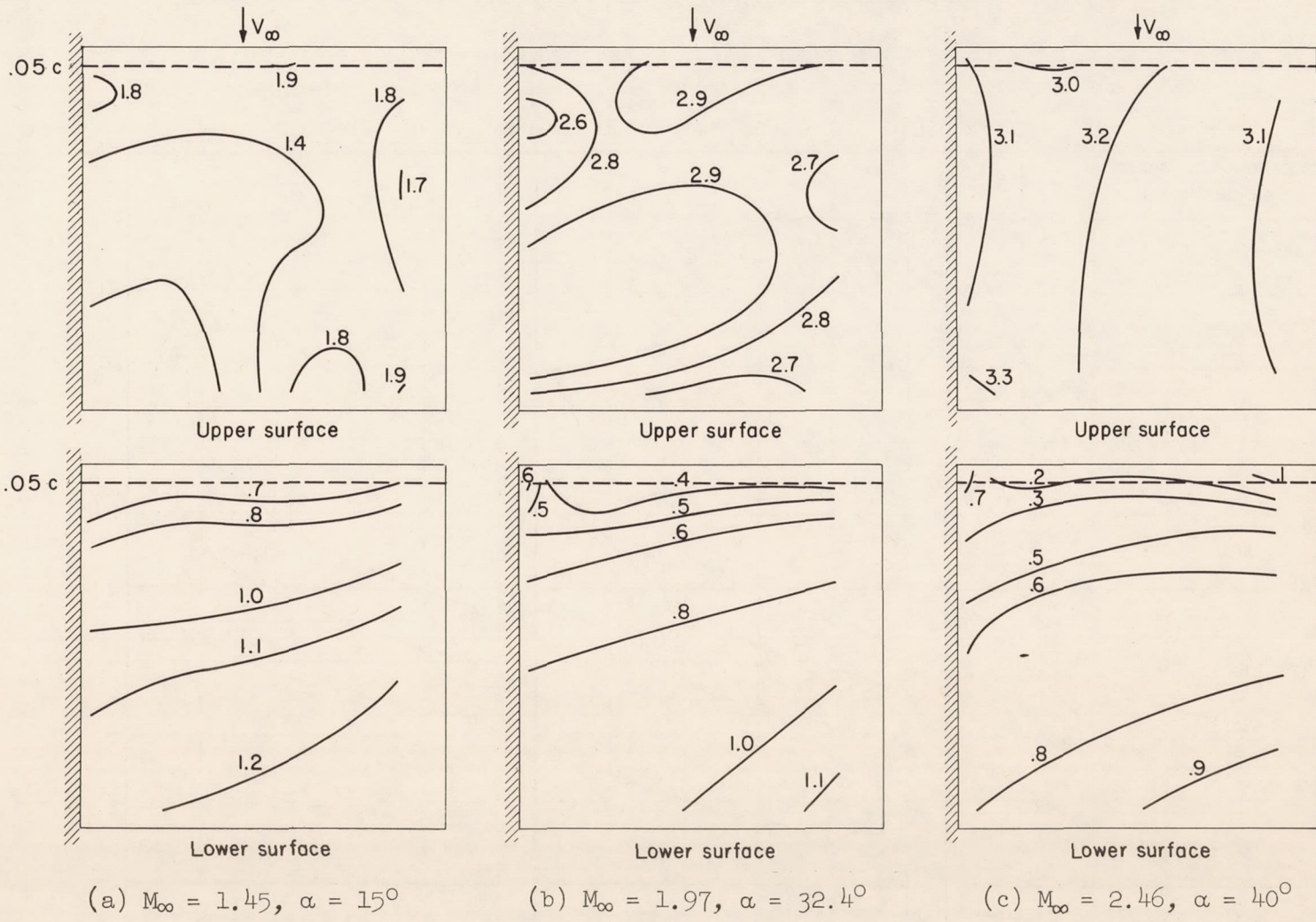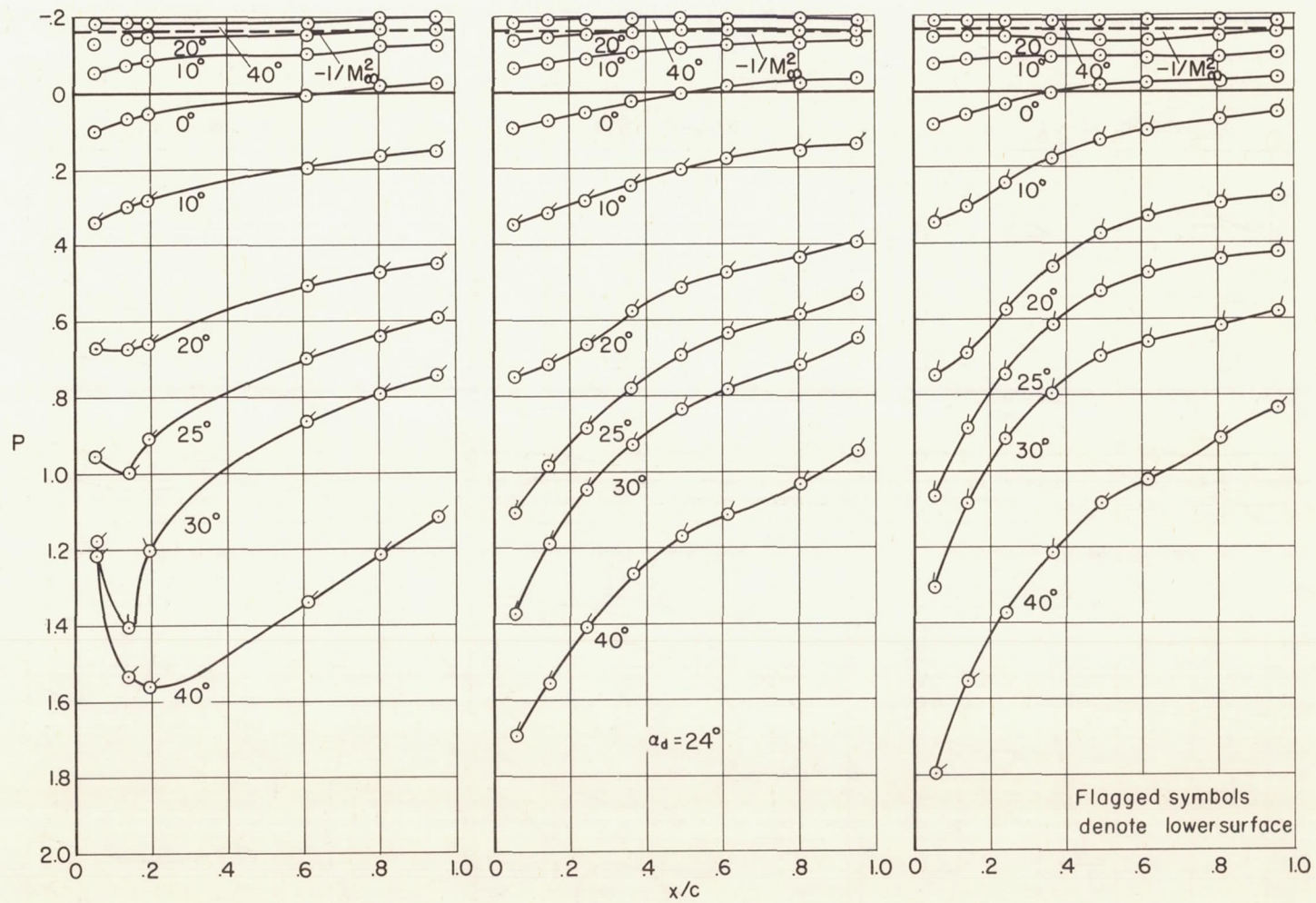leading-edge shock wave.

(a) $M_\infty = 1.45$, $\alpha = 15°$ (b) $M_\infty = 1.97$, $\alpha = 32.4°$ (c) $M_\infty = 2.46$, $\alpha = 40°$

Figure 18.- Mach number distribution on surfaces of rectangular wing on assumption stagnation streamline undergoes normal shock.
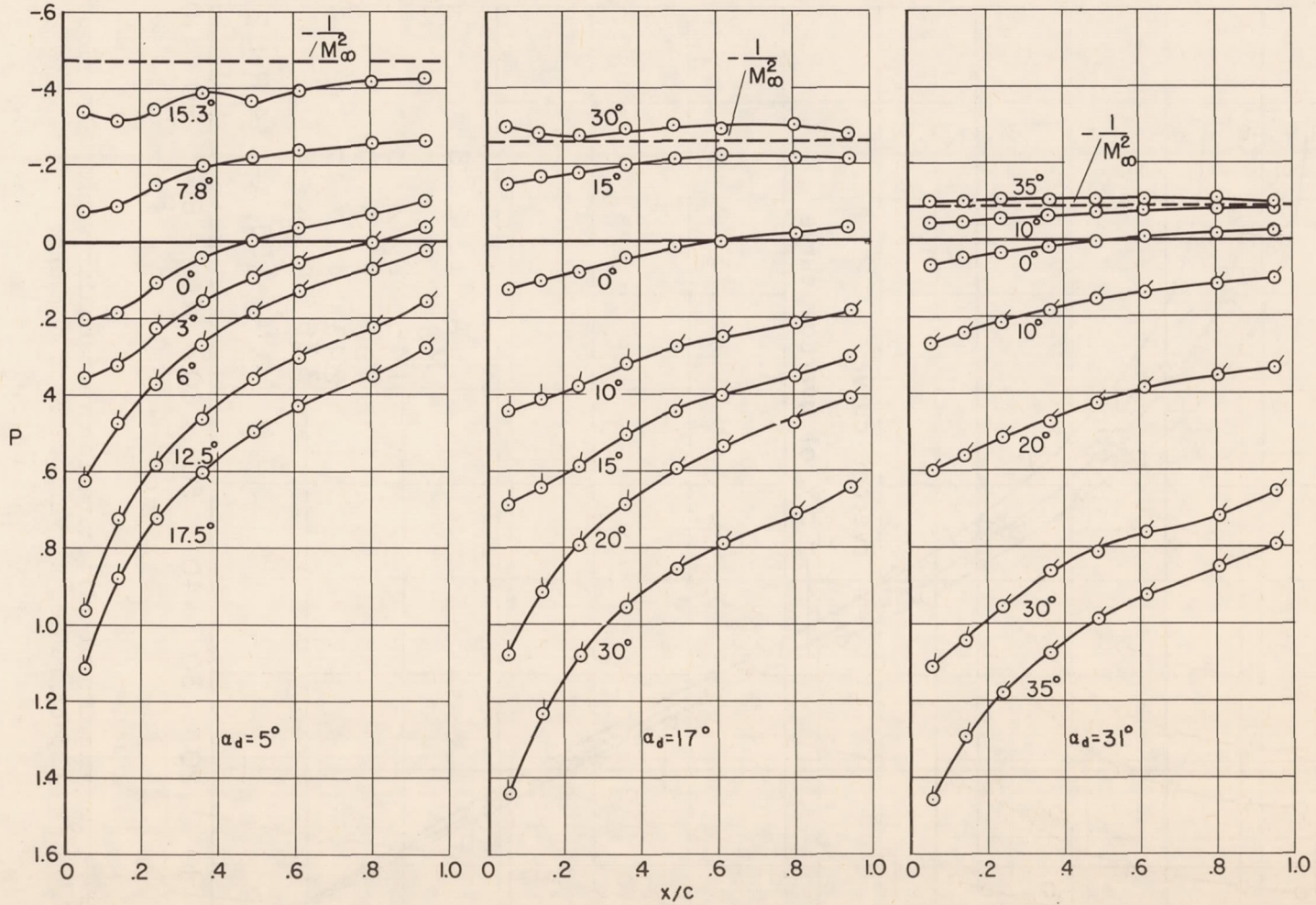
(a) $M_\infty = 2.46$, $y/s = 0.025$ (b) $M_\infty = 2.46$, $y/s = 0.250$ (c) $M_\infty = 2.46$, $y/s = 0.875$

Figure 19.- Pressure distribution on surface of rectangular wing; A = 2.

(d) $M_\infty = 1.45$, $y/s = 0.250$ (e) $M_\infty = 1.97$, $y/s = 0.250$ (f) $M_\infty = 3.36$, $y/s = 0.250$
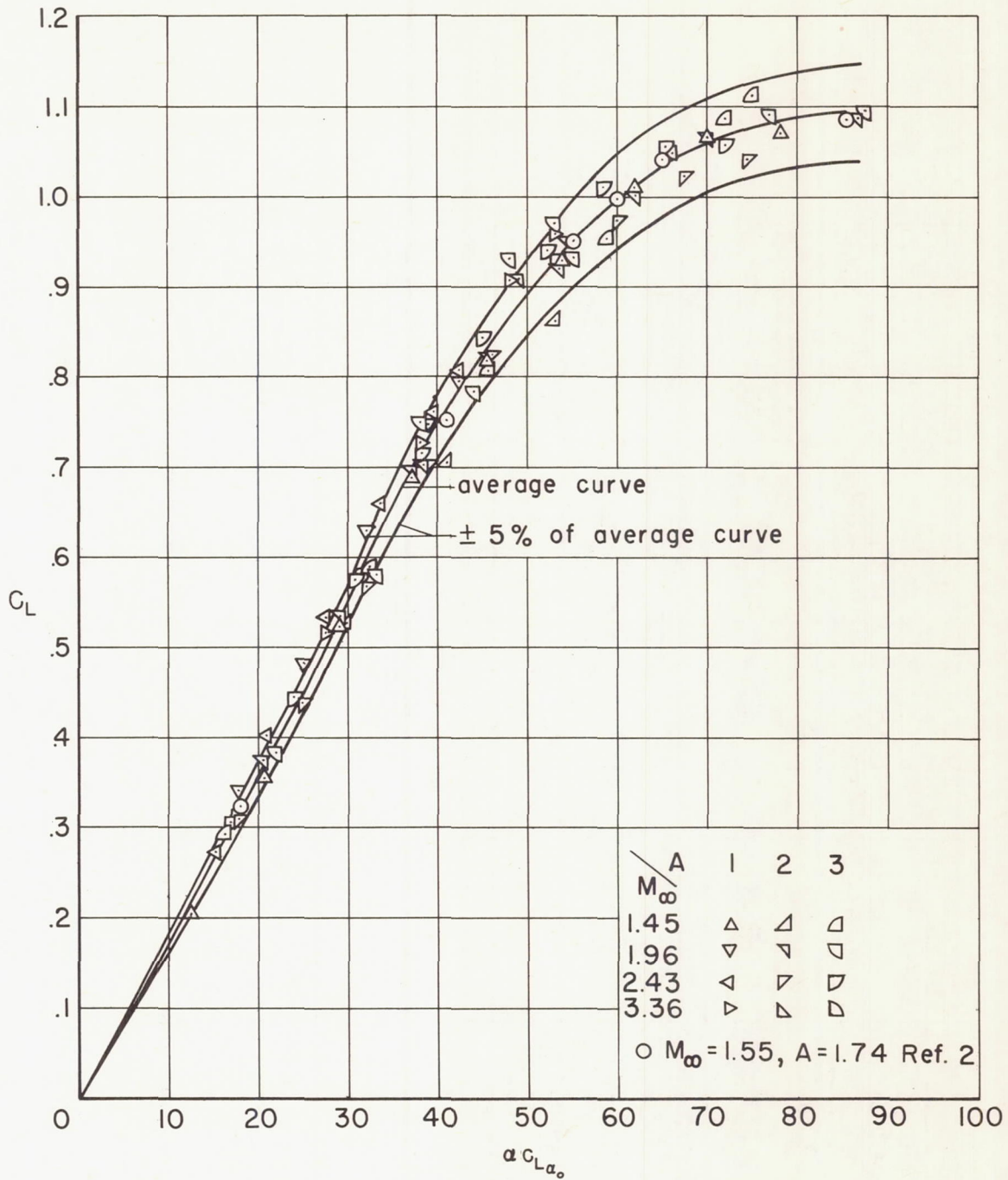
Figure 19.- Concluded.

Figure 20.- Correlation of lift data for rectangular wings of various aspect ratios at various Mach numbers.